

New perspectives in the use of the Ffowcs Williams–Hawkings equation for aeroacoustic analysis of rotating blades

By S. IANNIELLO

INSEAN – The Italian Ship Model Basin, Roma, Italy

(Received 25 October 2005 and in revised form 1 June 2006)

The Ffowcs Williams–Hawkings equation represents a standard approach in the prediction of noise from rotating blades. It is widely used for linear aeroacoustic problems concerning helicopter rotors and aircraft propellers and over the last few years, through the use of the so called *porous* (or *permeable*) surface formulation, has replaced the Kirchhoff approach in the numerical solution of nonlinear problems. Nevertheless, because of numerical difficulties in evaluating the contribution from supersonic sources, most of the computing tools are still unable to treat the critical velocities at which the shock delocalization occurs. At those conditions, the attention is usually limited to the comparison between the noise prediction and the experimental data in the narrow time region where the pressure peak value is located, but there has been little attention paid to the singular behaviour of the governing equation at supersonic speeds. The aim of this paper is to couple the advantages of the porous formulation to an emission surface integration scheme in order to show if and how the singularities affect the noise prediction and to demonstrate a practical way to remove them. Such an analysis enables an investigation of some interesting and somewhat hidden features of the numerical solution of the governing equation and suggests a new solution approach to predicting the noise of a rotor at any rotational velocity.

1. Introduction

The analysis of impulsive noise from rotating blades has been the subject of extensive theoretical and experimental work. Two different forms of impulsive noise are particularly relevant. One is known as blade vortex interaction (BVI) noise and mainly concerns the descent flight of an helicopter at a relatively low speed. In this case, the impulsive character of the noise signature is due to the fluctuating airload caused by the interactions of the blade with the shed tip vortex. The other is the high-speed impulsive (HSI) noise which primarily concerns the advancing blade of a helicopter rotor in level flight as well as the aircraft propellers operating at high tip speeds. There, the impulsive waveform arises from the high speed itself and the contribution of noise sources approaching (or experiencing) a supersonic speed. Both the phenomena are complex to model, but they differ greatly from both physical and numerical viewpoints. Numerically speaking, the prediction of BVI noise is more an *aerodynamic* than an *aeroacoustic* problem. The main difficulties concern the accuracy in computing the time-dependent blade pressure distributions, but the evaluation of the acoustic pressure in the far field is straightforward and can be obtained easily through the widely used linear formulae. In the estimation of the HSI noise, both the aerodynamic and the aeroacoustic aspects of the problem become

difficult to treat, since the fundamental contribution of nonlinear sources is related to complex noise generation and propagation mechanisms that take place in the flow field. Then, in addition to the difficulties of computing the requested aerodynamic data (pressure, density and the three-dimensional velocity field surrounding the blade at high transonic or supersonic speeds), we have to face the complex emission phenomena related to the high source speed.

Undoubtedly, the HSI noise represents one of the most annoying forms of noise generated by rotating blades. Its numerical prediction is made difficult by the occurrence of shock delocalization and the requirement of accounting for the particular behaviour of supersonic sources. Thus, in spite of the availability of different theoretical models and formulations, the calculations are often limited to subsonic source motion and it is not yet clear what is the best way to approach the problem. It is well-known that the (FW-H) equation published by Ffowcs Williams & Hawkings (1969) represents the governing equation of the aerodynamically generated sound. There, the contribution from the so-called quadrupole source terms is represented by three dimensional integrals theoretically extended to the whole region surrounding the body and affected by its motion. The evaluation of these volume integrals has always been considered a difficult and demanding task. Thus, the use of the FW-H equation has usually been limited to linear problems. Indeed, the volume integration can be easily and successfully applied up to the occurrence of the delocalization phenomena (Ianniello & De Bernardis 1994; Ianniello 1999*b*); it does not require any pre-processing on the computational fluid dynamics (CFD) input data and nowadays the issue of the computing effort seems to be rather questionable. Over the first half of the 1990s, the interest of the aeroacoustic community was focused on the Kirchhoff approach (Farassat & Myers 1988). By using an integration (control) surface placed far from the body and acting as a radiating domain, this method allows an overall noise prediction (from linear and nonlinear sources) through only surface integrals; then, the undesirable presence of volume terms is removed and a significant CPU time saving is obtained. Furthermore, the possible use of a non-rotating integration domain (enclosing the entire blade and the nonlinear source region) removes the singular behaviour due to supersonic sources motion and notably simplifies the numerical problems (Lyrintzis 1994; Strawn, Biswas & Lyrintzis 1996). Unfortunately, the main drawback of the Kirchhoff approaches is the close dependency of the numerical solution on the position of the control surface: if such a domain is placed in a region affected by the nonlinearities, the noise prediction can be completely unreliable (Brentner & Farassat 1997).

The use of the FW-H equation for nonlinear problems found a renewed interest among the aeroacousticians during the second half of the 1990s, when it appeared that this equation could provide a Kirchhoff-like solution. The method is known as *porous* (or *permeable*) formulation since it is a simple rewriting of the solving equation upon an integration surface placed far from the body, where the usual impermeability condition does not have to be applied. Although it is evidently similar to the Kirchhoff method, this approach always provides a physically correct estimation of the acoustic pressure and the location of the control surface represents merely a convergence parameter with respect to the contribution of the nonlinear terms. When the surface collapses upon the body, the impermeability condition automatically turns the porous formulation into the usual linear formula providing the well-known thickness and loading noise components. By progressively moving the surface far from the body, the contribution from the field (nonlinear) quadrupole sources is taken into account up to a converged solution. It is worth noting that the only formal differences between the porous formulation and a linear solver lie in the integral kernels and the requirement

for a larger set of input data (including the velocity and density distributions in addition to the pressure upon the surface). Then, the existing codes can be easily modified in order to extend their own capabilities and become a more general-purpose tools. Unfortunately, the favourable aspects of the porous formulation do not remove the main problems of the HSI noise prediction. When the shock delocalization requires the contribution of supersonic sources, the Doppler singularity prevents the use of standard retarded-time formulae and an alternative approach must be applied.

The appearance of singularities is a feature of the solution of the wave equation with sources moving at supersonic speeds. This behaviour is related to the occurrence of multiple emission times of supersonic sources and their own capability of turning from a single to a multi-emissive status within the revolution period. At these conditions, an accurate prediction of noise becomes difficult. Besides the direct consequences of the singularities, the step-by-step changes of the status of the sources produces an oscillating behaviour of numerical nature which is amplified by the presence of time derivatives outside the integral terms. Therefore, the computed waveforms can be heavily affected by numerical errors, or, in the worst case, completely unreliable. At present, not many numerical procedures can be used to approach this problem directly. Delrieux *et al.* (2003) used a fully non-compact integral formulation to compute the noise at the delocalized condition. The good agreement with the available experimental data proves the effectiveness of the procedure, but in spite of the absence of any singularity in the integral kernels and the use of a forward-in-time integration scheme, the resulting noise signatures are still affected by slight fluctuations. Moreover, some misleading conclusions are made about the choice of the integration domain and the possibility that noise prediction could somehow depend on it. Concerning this last aspect of the problem, Morgans *et al.* (2005) identifies as the best choice a cylindrical domain as close to the blade surface as possible while including all transonic flow regions. The calculations, limited to tip Mach numbers of 0.85 and 0.88, make use of a standard retarded time formulation (affected by the Doppler singularity) and do not allow us to extend the integration domain outside the sonic cylinder. Thus, at the highest rotational velocity, the numerical result exhibits a significant difference with respect to the experimental data and no indication is given as to the choice of a suitable integration domain in the supersonic region.

A possible way to account for the contribution of supersonic sources is to use an emission surface formulation, where at each observer time the manifolds traced by the retarded locations of the source points are assumed to be integration domains. Actually, these domains not only correspond to the emission surface Σ concerning the evaluation of the linear terms, but also to the emission volume \mathcal{V} related to the quadrupole sources, in which case the term *emission surface approach* is rather misleading. All the same, this formulation can account for the effects of multi-emissive sources through the numerical modelling of the time-dependent integration domains. From a computational point of view, the use of an emission surface formulation is not the easiest way to predict the noise but, at the same time, it appears to be the most effective and intuitive representation of the emission phenomena. For instance, it is easy to understand why a sweptback blade tip generates a reduced noise with respect to a rectangular tip by looking at the time evolution of the corresponding emission surfaces and the time-shifted contributions of the source points located in the tip region. Furthermore, the integral kernels related to the emission surface formula are simple to compute and are not affected by the Doppler singularity, thus removing the main restrictions due to the range of the rotational velocity. In spite of such unquestionable advantages, the emission surface formulation has rarely been

used because of the difficulties in constructing a supersonic retarded domain. The only available results at delocalized conditions were presented at the end of the 1990s. They refer to an approximated solution for the evaluation of the quadrupole noise only, where the calculations are limited to a two-dimensional flat mesh and to the far field, in plane observer locations (Farassat & Brentner 1998; Ianniello 1999*a, b*).

Within this context, the coupling between the emission surface approach (not affected by the Doppler singularity) and the porous formulation (including the nonlinear terms contribution through a suitable choice of the control surface) could reasonably provide a superior approach to the problem of HSI noise prediction. Such an approach could also clarify some interesting and little known aspects of the emission phenomena and the corresponding numerical solutions. For instance, the aeroacoustic analysis of rotors operating at supersonic tip speed still represents an open question. The few pressure time histories available in the literature date back to twenty years ago and are often limited to a thickness noise estimation (Farassat, Pegg & Hilton 1975; Farassat, Padula & Dunn 1987; Amiet 1988; Wells 1991). At those conditions, the numerical predictions of noise are heavily affected by a singular behaviour and exhibit some abrupt changes of the pressure waveforms which have been only partially explained.

Another issue concerns the numerical behaviour of the integral kernels at supersonic speed. In the emission surface formulation, the Doppler factor does not appear in the quadrupole (volume) integrals, whereas within the thickness and loading (surface) integrals it is replaced by another factor, $\Lambda = (1 - 2M_n \hat{\mathbf{n}} \cdot \hat{\mathbf{r}} + M_n^2)^{1/2}$ (where $\hat{\mathbf{n}}$ and $\hat{\mathbf{r}}$ represent the unit vectors in the outward normal with respect to the surface and the radiation directions, respectively) which makes these terms 'less' singular. In fact, in this case, the singularity appears only when M_n (the projection of the Mach number along $\hat{\mathbf{n}}$) is equal to 1 and, at the same time, $\hat{\mathbf{n}}$ is aligned along the source observer direction. Many workers recognized Λ as a non-integrable singularity, but a numerical investigation into its own behaviour has never been carried out. From a theoretical standpoint, the problem was exhaustively treated by Farassat who developed some complex formulations in an attempt to provide a numerical answer to the matter. Farassat concluded that the insertion of the quadrupole sources contribution into the overall solution removes the singular behaviour due to the Λ term. Nonetheless, to my knowledge, no numerical demonstration of such an assertion has ever been shown, except for some academic test cases (Farassat & Farris 1999). Since the integral kernels corresponding to the porous formulation include the Λ term and, at the same time, can account for the contribution of the quadrupole sources, the use of an emission-porous surface formulation outside the sonic cylinder should clarify the role played by the Λ singularity.

The numerical construction of a supersonic emission surface is not an easy task. The multiple emission times cause the occurrence of unconnected patches which temporarily link together and then disappear. This complex time evolution strongly depends on the kinematics of the problem and the geometry of the numerical mesh; thus, a solver devoted to modelling the time-dependent Σ surface has to be flexible and robust enough to manage the different topologies of the CFD meshes. Moreover, the calculations must be repeated at each observer location and usually require great accuracy: any irregularity can have devastating consequences on the resulting waveforms. In order to treat these problems suitably and to implement the emission-porous surface formulation, a new version of the \mathcal{K} -algorithm (Ianniello 1999*a, b*) has been developed. This procedure was conceived at the end of the 1990s in order to estimate the problematic quadrupole source term through an approximate formulation

proposed by Brentner (1997). Based on the key idea of classifying the retarded spanwise sections of a structured grid on the grounds of well-established *identification criteria*, the algorithm proved to be very effective in the numerical treatment of delocalized conditions. Nonetheless, the criteria used to identify the retarded sections were much too restrictive and somewhat oriented towards symmetrical configurations. Here, these limitations have been removed. Therefore, we are now in a position to perform these kinds of calculations and to throw new light upon the numerical solution of such challenging problems.

The structure of the paper is as follows. Section 2 is devoted to the theoretical background; it presents all the equations used throughout the paper, describes the numerical problems related to the high-speed emission phenomena and summarizes the main features of the different solution approaches. Section 3 tests the \mathcal{H} -algorithm and its own capability to construct a supersonic emission surface through two interesting and unrealistic test-cases. In §4, the effectiveness of the emission-porous surface formulation is tested on a critical HSI noise test-bed, with a comprehensive convergence analysis. The relations between the Λ singularity and the emission surface and the effects of the singular behaviour on noise prediction are extensively treated in §4.1. Then, the attention is focused on the evaluation of a supersonic thickness noise and a general discussion on the numerical solution of the FW-H equation at supersonic speeds is proposed (§4.2). Subsequently, a strategic choice of the integration domain aimed at removing the numerical singularities and reducing the computational effort is addressed and two new solution approaches are proposed. The first enables the evaluation of the HSI noise by a singularity-free equation (§4.3), whereas the second (strictly valid for in-plane observer locations only) allows us to reduce the calculations to a simple line integral (§4.4). Finally, §5 summarizes the main conclusions of the paper, while the Appendix reveals some fundamental features of the \mathcal{H} -algorithm and the key ideas developed to model a supersonic emission surface numerically.

2. Theoretical background

The Ffowcs Williams–Hawkings equation represents an elegant manipulation of the fundamental conservation laws of mass and momentum which gives rise to the following inhomogeneous wave equation written in terms of generalized functions

$$\begin{aligned} \bar{\square}^2 p'(\mathbf{x}, t) = & \frac{\bar{\partial}}{\partial t} \{ [\rho_0 v_n + \rho(u_n - v_n)] \delta(f) \} \\ & - \frac{\bar{\partial}}{\partial x_i} \{ [\Delta P_{ij} \hat{n}_j + \rho u_i(u_n - v_n)] \delta(f) \} + \frac{\bar{\partial}^2}{\partial x_i \partial x_j} \{ T_{ij} H(f) \}. \end{aligned} \quad (2.1)$$

The equation $f=0$ is an implicit equation which describes an arbitrary surface, whose choice heavily affects the physical meaning of the different terms. The fluid and surface velocity components are indicated by u_i and v_i , respectively, $\tilde{\rho} = \rho - \rho_0$ is the density perturbation with respect to the undisturbed medium and the subscript n denotes the projection along the outward normal to the surface. The D'Alembert operator is given by $\bar{\square}^2 = [(1/c_0^2)\bar{\partial}^2/\partial t^2] - \bar{\nabla}^2$, the Lighthill tensor is $T_{ij} = \rho u_i u_j + P_{ij} - c_0^2 \tilde{\rho} \delta_{ij}$, where c_0 is the sound speed in the undisturbed medium; P_{ij} represents the compressive stress tensor and $\Delta P_{ij} = P_{ij} - p_0 \delta_{ij}$, δ_{ij} being the Kronecker symbol.

The presence of the Dirac and Heaviside functions shows the different nature of the source terms: two surface terms directly related to the effects of the discontinuity $f=0$ in the flow field and a volume term accounting for all sources acting outside

the surface $f=0$. When $f=0$ coincides with the body surface S , the impermeability condition $u_n = v_n$ simplifies the equation (2.1) and the use of the Green's function approach leads to the following integral form

$$\begin{aligned}
 4\pi p'(\mathbf{x}, t) = & \frac{\partial}{\partial t} \int_S \left[\frac{\rho_0 v_n}{r|1 - M_r|} \right]_{\tau} dS + \frac{1}{c_0} \frac{\partial}{\partial t} \int_S \left[\frac{\tilde{p} \hat{\mathbf{n}} \cdot \hat{\mathbf{r}}}{r|1 - M_r|} \right]_{\tau} dS \\
 & + \int_S \left[\frac{\tilde{p} \hat{\mathbf{n}} \cdot \hat{\mathbf{r}}}{r^2|1 - M_r|} \right]_{\tau} dS + \frac{1}{c_0^2} \frac{\partial^2}{\partial t^2} \int_V \left[\frac{T_{rr}}{r|1 - M_r|} \right]_{\tau} dV \\
 & + \frac{1}{c_0} \frac{\partial}{\partial t} \int_V \left[\frac{3T_{rr} - T_{ii}}{r^2|1 - M_r|} \right]_{\tau} dV + \int_V \left[\frac{3T_{rr} - T_{ii}}{r^3|1 - M_r|} \right]_{\tau} dV. \quad (2.2)
 \end{aligned}$$

This equation is written under the assumptions of an inviscid flow (thus reducing the compressive stress tensor to the scalar pressure field on the blade surface: $\Delta P_{ij} = (p - p_0)\delta_{ij} = \tilde{p}\delta_{ij}$) and isentropic transformations, for which the pressure–density relationship can be approximated by the linear term of its series expansion (i.e. $p' = c_0^2 \tilde{p}$, where p' denotes the acoustic pressure disturbance). The V domain represents the three-dimensional space (outside of $f=0$) where the presence of the moving body affects the state of the medium; r is the source–observer distance, and $\hat{\mathbf{n}}, \hat{\mathbf{r}}$ are the unit vectors in the outward normal (with respect to S) and the radiation directions, respectively. All the integral kernels are evaluated at the emission (retarded) time τ which represents, for any observer time t and location \mathbf{x} , the instant when the contribution to the noise signature was released. The difference between t and τ is known as the *compressibility delay* and represents a fundamental feature of the acoustic integrals: it emphasizes that sound propagates in the flow field at a finite speed. Equation (2.2) is usually identified as the *retarded time formulation* (Brentner & Farassat 2003) and is well known among the aeroacousticians. By limiting the computations to the surface terms (known as thickness and loading noise) and if the time derivatives are taken inside the integrals, the result is Farassat's *formulation 1A* (Farassat 1981), the standard retarded-time formula for rotating-blade problems. The implementation of this formula is straightforward and can be realized in different ways. In particular, it is possible to use a *forward-* or a *backward-in-time* integration scheme. In the first case, the observer time t is assumed to be unknown and by moving forward in time (starting from a prescribed emission time τ) the resulting noise signature is obtained through an interpolation of the different, time-shifted sources' contributions. Alternatively, by fixing the instant t , it is possible to go backward in time to compute the corresponding τ and the retarded integral kernels. Because of the blade rotational motion, this computation requires an iterative procedure (see the Appendix). The evaluation of the volume terms (the quadrupole noise) is not as easy; it requires the knowledge of the flow-field velocity, pressure and density, and a three-dimensional integration. Furthermore, the quadrupole sources contribution becomes significant at high transonic speed when the Doppler singularity $|1 - M_r|$ also affects the reliability of the numerical solution. The singular behaviour concerns the supersonic sources which can experience a multi-emissive status within the revolution period: for a supersonic source, the signatures released at different positions y_i (corresponding to multiple emission times τ_i by the same source point) can reach the observer location \mathbf{x} (at time t) simultaneously. This lack of a one-to-one correspondence between the observer and emission times depends on the source speed and the relative source–observer position. From a mathematical standpoint, there exists an integral formulation which makes this fundamental aspect of the problem explicit. By suitably manipulating the original four-dimensional integrals

provided by the Green's function method, the integral formulation takes the form

$$\begin{aligned}
 4\pi p'(\mathbf{x}, t) = & \frac{\partial}{\partial t} \int_{\Sigma} \left[\frac{\rho_0 v_n}{r\Lambda} \right]_{\tau} d\Sigma + \frac{1}{c_0} \frac{\partial}{\partial t} \int_{\Sigma} \left[\frac{\tilde{p} \hat{\mathbf{n}} \cdot \hat{\mathbf{r}}}{r\Lambda} \right]_{\tau} d\Sigma + \int_{\Sigma} \left[\frac{\tilde{p} \hat{\mathbf{n}} \cdot \hat{\mathbf{r}}}{r^2\Lambda} \right]_{\tau} d\Sigma \\
 & + \frac{1}{c_0^2} \frac{\partial^2}{\partial t^2} \int_{\mathcal{V}} \left[\frac{T_{rr}}{r} \right]_{\tau} d\mathcal{V} + \frac{1}{c_0} \frac{\partial}{\partial t} \int_{\mathcal{V}} \left[\frac{3T_{rr} - T_{ii}}{r^2} \right]_{\tau} d\mathcal{V} + \int_{\mathcal{V}} \left[\frac{3T_{rr} - T_{ii}}{r^3} \right]_{\tau} d\mathcal{V}
 \end{aligned} \quad (2.3)$$

As already mentioned, $\Lambda = (1 - 2M_n \hat{\mathbf{n}} \cdot \hat{\mathbf{r}} + M_n^2)^{1/2}$ while Σ and \mathcal{V} represent the emission domains traced by the retarded location(s) $\mathbf{y}(\tau)$ of the source points. For this reason, equation (2.3) which usually includes only the surface terms is known as the *emission surface formulation*. Note that the occurrence of multiple emission times is taken into account through the time-dependent integration domains so that the Doppler singularity disappears from all the integral kernels. Nonetheless, the surface terms are still affected by the singular value $\Lambda = 0$, occurring when M_n and $\hat{\mathbf{n}} \cdot \hat{\mathbf{r}}$ are simultaneously equal to $+1$ or -1 . The evaluation of time-dependent integration domains notably increases the computing effort so that, at subsonic source speed, the use of equation (2.3) is not as computationally efficient as formulation 1A in the prediction of thickness and loading noise. Regarding the volume terms, the evaluation of \mathcal{V} may be considered as an academic exercise rather than a practicable solution and is strictly limited to conditions below delocalization. In fact, the occurrence of multi-emissive sources makes the evaluation of a supersonic \mathcal{V} a very demanding task. The most practical way to manage the volume terms of equation (2.3) outside the sonic cylinder is to perform a preliminary integration along a suitable direction in order to approximate them into some surface integrals. This procedure, originally proposed by Yu, Caradonna & Schmitz (1978) and revisited by Farassat & Brentner (1988), is known as *far-field approximation* and has been successfully applied in the HSI noise prediction (Farassat & Brentner 1998*a, b*; Ianniello 1999*a, b*). By assuming the quadrupole source strength

$$Q_{ij} = \int_{n_q} T_{ij} dn_q, \quad (2.4)$$

the three-dimensional integrals of equation (2.3) can be rewritten in the form

$$\begin{aligned}
 4\pi p'_Q(\mathbf{x}, t) = & \frac{1}{c_0^2} \frac{\partial^2}{\partial t^2} \int_{\Sigma_q} \left[\frac{Q_{rr}}{r} \right]_{\tau} d\Sigma_q \\
 & + \frac{1}{c_0} \frac{\partial}{\partial t} \int_{\Sigma_q} \left[\frac{3Q_{rr} - Q_{ii}}{r^2} \right]_{\tau} d\Sigma_q + \int_{\Sigma_q} \left[\frac{3Q_{rr} - Q_{ii}}{r^3} \right]_{\tau} d\Sigma_q.
 \end{aligned} \quad (2.5)$$

In practice, equation (2.4) approximates the Lighthill tensor contribution by an equivalent source distribution on a flat mesh S_q placed on the rotor disk and suitably extended ahead of the leading edge, behind the trailing edge and off the blade tip in order to account for the delocalized noise sources. The S_q mesh is characterized by the outward normal direction n_q and corresponds to the emission domain Σ_q appearing in (2.5). Note that this equation does not exhibit any singularity, thus it appears to be the most practicable way to determine the quadrupole source terms of the FW-H equation at supersonic speed (provided the supersonic Σ_q surface can be constructed). Unfortunately, the basic assumptions of the far-field approximation are rather restrictive. The use of equation (2.4) assumes the equality of the emission times at sources symmetrically placed with respect to S_q and collapses all data along

n_q into a single point. These assumptions can be considered valid only in the rotor plane and at far-field observer locations, so that the evaluation of the quadrupole noise at delocalized conditions and out of the rotor plane still represents an open question.

The porous formulation consists of integrating the fundamental equation (2.1) on a surface S_p placed far from the body, where the usual impermeability boundary condition does not have to be applied. Although such a method had already been treated by Ffowcs Williams & Hawkings (1969), it was first implemented for rotors by Di Francescantonio (1997), by assuming

$$U_i = \left(1 - \frac{\rho}{\rho_0}\right) v_i + \frac{\rho}{\rho_0} u_i, \quad (2.6)$$

$$L_i = P_{ij} \hat{n}_j + \rho u_i (u_n - v_n). \quad (2.7)$$

In this manner equations (2.2) and (2.3) are formally not altered and give rise to the following solving formulae

$$4\pi p'(\mathbf{x}, t) = \frac{\partial}{\partial t} \int_{S_p} \left[\frac{\rho_0 U_n}{r|1 - M_r|} \right]_{\tau} dS_p + \frac{1}{c_0} \frac{\partial}{\partial t} \int_{S_p} \left[\frac{L_r}{r|1 - M_r|} \right]_{\tau} dS_p + \int_{S_p} \left[\frac{L_r}{r^2|1 - M_r|} \right]_{\tau} dS_p + p'_Q(\mathbf{x}, t), \quad (2.8)$$

$$4\pi p'(\mathbf{x}, t) = \frac{\partial}{\partial t} \int_{\Sigma_p} \left[\frac{\rho_0 U_n}{r\Lambda} \right]_{\tau} d\Sigma_p + \frac{1}{c_0} \frac{\partial}{\partial t} \int_{\Sigma_p} \left[\frac{L_r}{r\Lambda} \right]_{\tau} d\Sigma_p + \int_{\Sigma_p} \left[\frac{L_r}{r^2\Lambda} \right]_{\tau} d\Sigma_p + p'_Q(\mathbf{x}, t), \quad (2.9)$$

where Σ_p represents the retarded domain corresponding to the S_p porous surface. The term $p'_Q(\mathbf{x}, t)$ still indicates the noise contribution of the field quadrupole sources in the region *outside the $f=0$ domain*. Thus, if the control surface S_p is suitably placed in order to include all the sound sources, the contribution $p'_Q(\mathbf{x}, t)$ tends to zero and an overall noise prediction is achievable through the computation of surface integrals only. Note that by moving S_p in the flow field, the surface source terms lose their physical meaning of thickness and loading noise related to the fluid displacement and airload distribution caused by body motion. Then, in the following, we will refer to these terms as to *pseudo-thickness* and *pseudo-loading* terms.

The porous formulation represents the most suitable and effective way to solve the FW-H equation. Equation (2.8) is generally adopted in a form analogous to formulation 1A by inserting the time derivatives into the integral sign, but suffers the well-known limitations due to the Doppler singularity. On the contrary, because of the difficulties in constructing the emission surface Σ_p outside the sonic cylinder, equation (2.9) has never been used. Nonetheless, it represents a comprehensive solution of the FW-H equation, free from the Doppler singularity and volume integral terms, which could be theoretically used at any range of the rotational velocity. We will refer to this equation as to the *emission-porous surface formulation*. The main drawbacks of such an equation are the requirement of modelling a supersonic emission surface and the presence of the $\Lambda=0$ singularity: in the following sections it will be explained how to address both of these problems.

3. The \mathcal{H} -algorithm

The \mathcal{H} -algorithm is a procedure conceived to model the time evolution of a supersonic Σ surface for a rotating body. Starting from a structured numerical mesh where it is possible to identify a fixed number of spanwise sections, the basic idea is to use some well-established identification criteria aimed at classifying their own retarded configurations. In this manner, the emission domain can be divided into a finite number of homogeneous patches composed of sections of the same type. This procedure enables modelling of the unconnected regions occurring and collapsing in the field, owing to the appearance and disappearance of multiple emission times and corresponding to the single- and multi-emissive status of the supersonic sources. At each time step, the noise is determined as the sum of the integral terms computed on each patch. Since the acoustic pressure is related to a time derivative of the integral terms, great accuracy is required in the calculation of the $\Sigma(t)$ function. Then, whatever the resolution of the starting mesh may be, the algorithm must adopt a step-by-step refinement of the mesh, both along the spanwise direction (to model the boundaries of the adjoining patches) and the chordwise direction (to account suitably for the multi-emissive status of supersonic sources).

The first version of the algorithm was developed to evaluate the HSI noise for a typical test bed (the UH-1H non-lifting, hovering rotor and an in-plane observer) through the far-field approximation in the form proposed by Brentner (1997). The noise predictions exhibited a good agreement with the available experimental data (Ianniello 1999*a, b*). They confirmed both the capability of the procedure to model the Σ domain accurately outside the sonic cylinder and the effectiveness of the emission surface formulation (although in an approximated solving form) in the numerical treatment of delocalized conditions. Subsequently, the algorithm was modified in order to treat some different blade geometries and to reduce the requested CPU time (Ianniello 2001). Nevertheless, the criteria used to identify the possible retarded configurations of the spanwise sections (strictly related to the change of curvature of Σ) limited the range of applicability to symmetrical problems. The criteria did not allow the modelling of the time evolution of the emission surface during the whole revolution period. They could manage only open sections, where it was possible to identify a leading and a trailing edge unambiguously. Recently, the \mathcal{H} -algorithm has been thoroughly revisited in order to overcome these restrictions. The present version removes any limit about the number of branches corresponding to a retarded and fragmented section: it does not link the identification criteria to any geometrical condition occurring during the revolution. Thus, it is possible to consider asymmetrical configurations, with complex geometries and observers placed out of the rotational plane. The only restriction concerns the number of emission times for each source (limited to 3), although the procedure could even be extended to account for a higher value.

The computation of a supersonic Σ surface is a complex problem. Great care must be used to model the emission domain correctly and to avoid any numerical fluctuation in the resulting noise waveform. A description of the different strategies used to address the problem is given in the Appendix. In order to show the robustness of the algorithm in modelling a supersonic emission domain, two critical and unrealistic test cases are examined. A sketch of the test configurations is drawn in figure 1. The first problem refers to a sphere with a diameter of 2 m, centred at (0, 1.5, 0) and rotating counterclockwise at a velocity of approximately 5500 r.p.m.; this value corresponds to a Mach number at the inner and outer (spanwise) sections of 0.84 and 4.23, respectively. The numerical mesh is 40×101 (number of sections \times number of nodes at each section) and is not stretched. A spherical geometry at such a high rotational

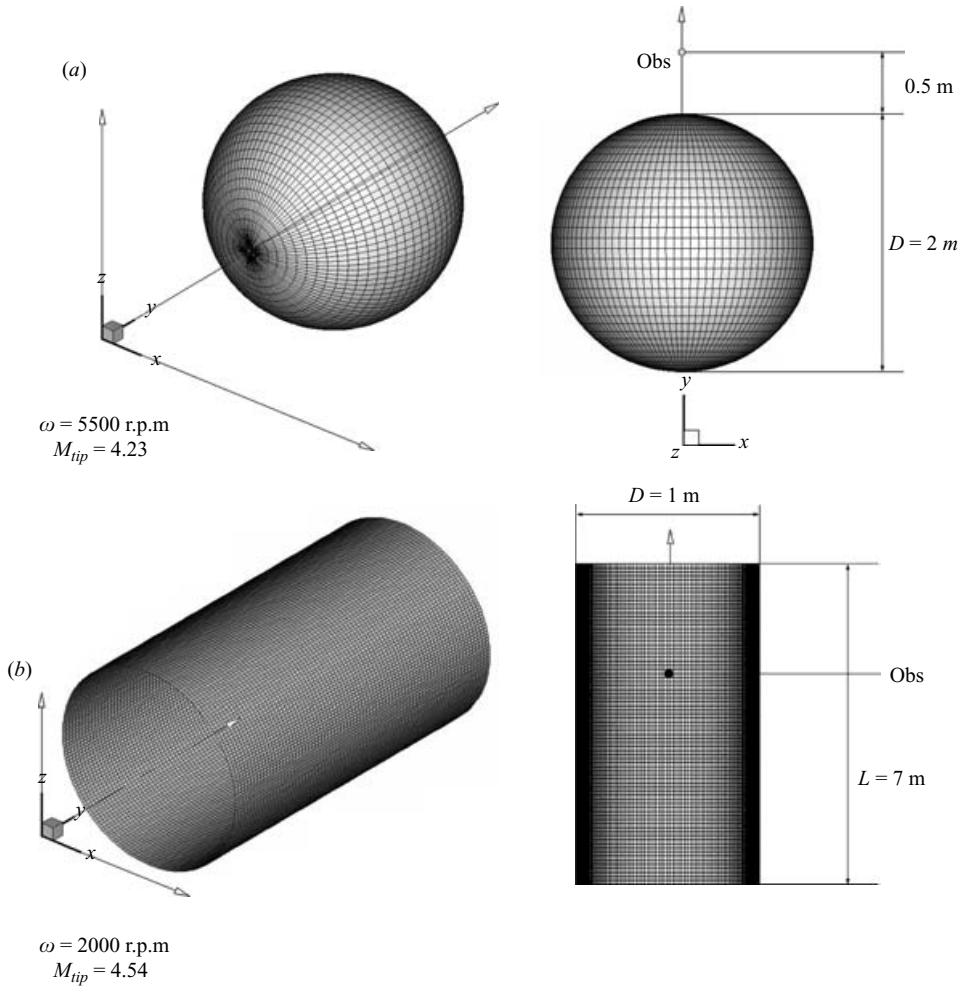


FIGURE 1. The two configurations proposed to test the capability and robustness of the \mathcal{K} -algorithm in modelling a supersonic emission surface.

speed represents a difficult test case for the numerical procedure since the emission surface undergoes an impressive deformation and exhibits a complex multiconnected shape. The observer is placed in the $Z=0$ symmetry plane at $(3, 0, 0)$, very close to the ‘tip’ section. The second test case concerns an open cylinder with a length of 7 m, a radius of the circular section of 4 m and discretized through an 80×201 mesh. The rotational velocity is set to 2000 r.p.m. so that the whole body experiences a supersonic speed (in a range of the Mach number between 1.23 at the hub and 4.54 at the tip). The most anomalous aspect of this test, however, is the observer located at $(4, 0, 0.5)$, a point intersected by the body’s trajectory. Note that the out-of-plane position gives rise to a heavily fragmented and asymmetrical emission surface. Thus, the identification criteria used to recognize the different integration patches are severely tested.

Figure 2 depicts the emission surfaces corresponding to the sphere at two subsequent time steps. In figure 2(a), Σ consists of two unconnected domains, whereas figure 2(b) shows a single manifold with a complex shape, characterized by both convex and

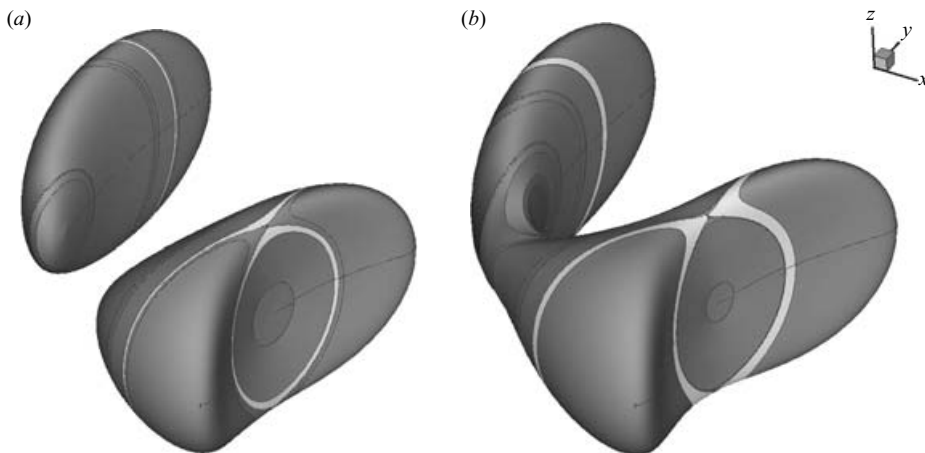


FIGURE 2. Emission surfaces corresponding to the supersonic sphere of test case 1. The observer is located in the $Z=0$ plane of symmetry, at half a metre from the tip section. The light regions point out the complex topology assumed by some integration patches, while the curves depicted upon the surfaces represent the boundaries of the patches.

concave regions. The black lines show the boundaries of the different integration patches determined by the algorithm. The most interesting aspect of figure 2 is that the light patches, composed by three separate branches, correspond to spanwise sections where not all the source points have multiple emission times. Such a configuration was not included among the possibilities taken into account by the old version of the algorithm and prove the effectiveness of the present identification criteria.

Figure 3 shows a sequence of six time steps for test case 2, approximately corresponding to the intersection of the emission surface with the observer location. In order to appreciate the evolution of some hidden regions, a portion of the rendered surface has been depicted with a different greyscale and a higher level of translucency. Still, the lines correspond to the boundaries of the integration patches and point out the accuracy of the implemented step-by-step mesh refinement process (Appendix). A sort of spherical hollow centred at the observer appears inside the emission domain (figure 3a) and grows (figure 3b–d) up to provide a toroidal three-dimensional manifold (figure 3e, f). Let us note that the out-of-plane observer position makes the configuration asymmetrical: the inner cavity connects to the upper region of Σ (figure 3c) while the lower one is still separated from it. The complexity of these configurations and the capability of the algorithm in modelling the corresponding emission surface provides confidence to face the problem of evaluating the surface integrals of equation (2.9).

4. Numerical results

In order to show the capability of the emission-porous surface formulation in the numerical prediction of noise, we will focus our attention on the critical test-bed of the UH-1H non-lifting hovering rotor at $M_{tip} = 0.95$, for which a set of experimental data is available. The pronounced shock delocalization occurring at such an operating condition allows a deep consideration of the numerical aspects we are interested in and allows us to test the robustness and reliability of the new \mathcal{H} -algorithm. The necessary aerodynamic input is provided by an Euler code (Kuntz *et al.* 1995).

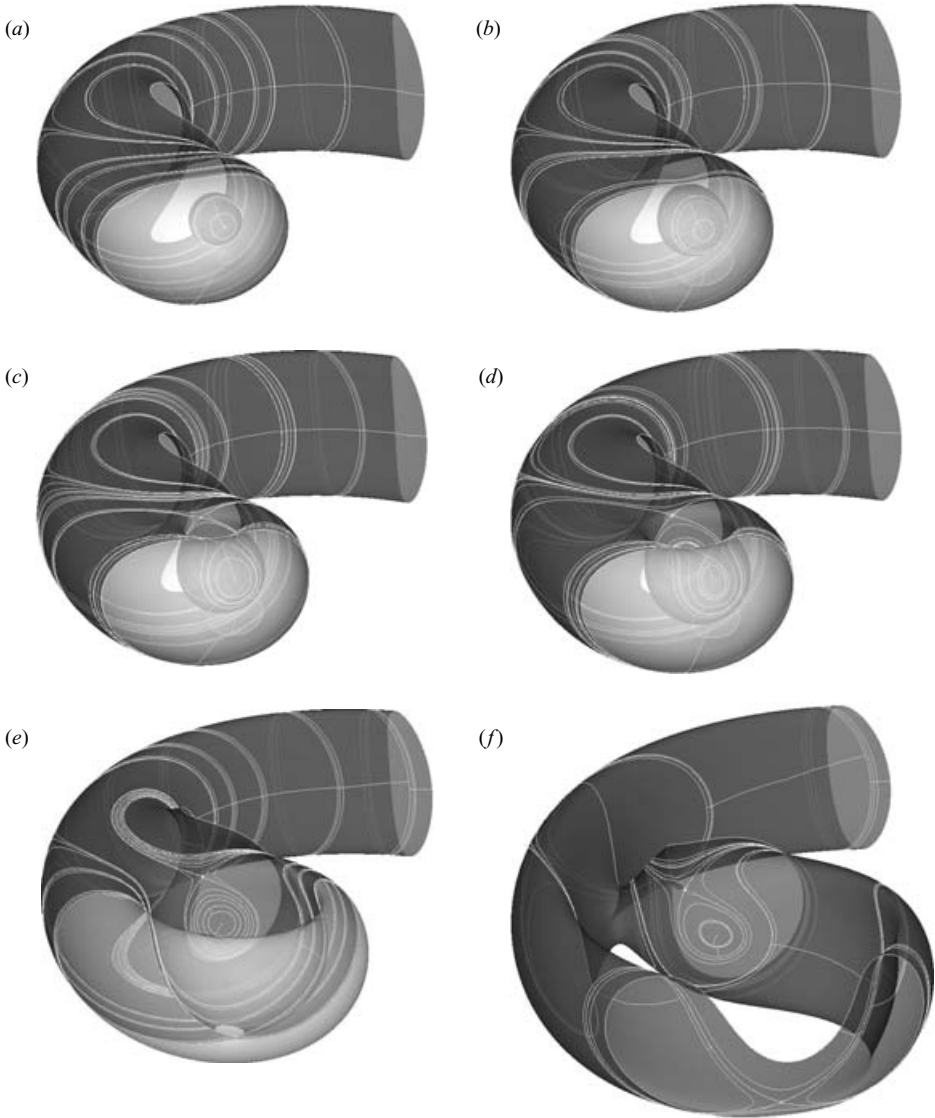


FIGURE 3. Emission surfaces corresponding to the supersonic cylinder of test case 2. The spheroidal cavity at (a) is centred at the out-of-plane observer location; it grows in the subsequent time steps to provide a sort of toroidal surface.

The numerical mesh is composed of 41 layers in the direction normal to the rotor disk, 97 sections along the span and 129 nodes chordwise. It exhibits a pronounced sweep and extends significantly beyond the sonic cylinder. The chordwise distribution of nodes is not uniform and depends on the shock-capturing procedure implemented in the aerodynamic solver. Moreover, each grid layer widens moving towards the sweptback tip region, thus assuming a rather irregular cylindrical shape. The blade chord is $c = 0.0762$ m and the observer is located in the $Z = 0$ plane of symmetry, at a distance of $3.09R$ from the rotor hub (the rotor radius $R = 1.045$ m). A three-dimensional sketch of the numerical grid is shown in the figure 4(b), where only the first ($k = 1$) and the last ($k = 41$) layers have been drawn for clarity. The top-view

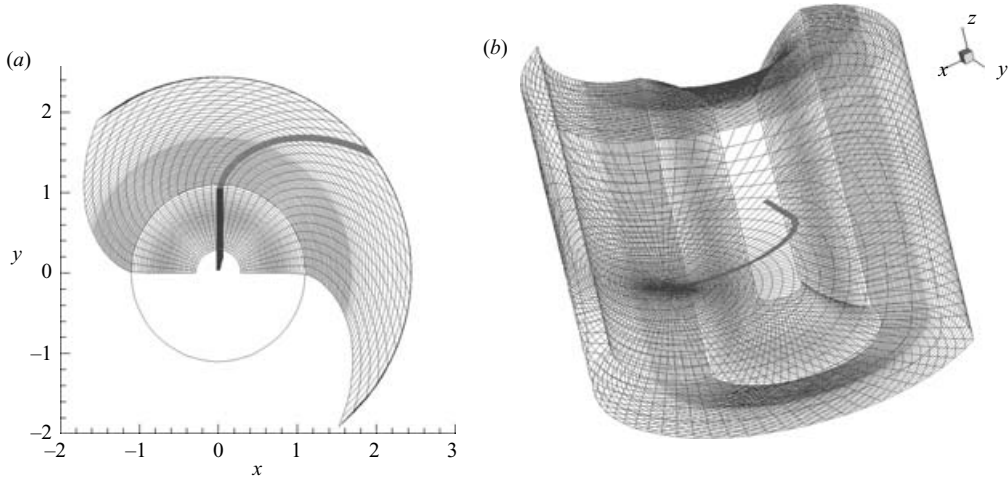


FIGURE 4. (a) Top and (b) three-dimensional views of the CFD Euler mesh used for calculations. For clarity, only the first ($k = 1$) and last ($k = 41$) grid layers are shown; (a) shows the position of the blade and the sonic cylinder corresponding to a blade tip Mach number of 0.95.

(figure 4a) highlights the position of the blade within the first layer and the corresponding sonic cylinder. Despite the complex topological features of the CFD grid, no interpolation has been carried out on the aerodynamic data in order to avoid any further approximation and to test the code’s capability in managing an irregular mesh.

The comparison between the available experimental data and the noise prediction provided by the emission-porous surface formulation is reported in figure 5(b). The agreement is very good: both the negative peak pressure value and the typical asymmetrical waveform are well captured. Some minor differences, concerning the width of the signature and the recompression positive peak value, are attributable to the numerical nature of the input data. Figure 5(a) shows the integration domain used for calculations. It corresponds to the $k = 35$ layer of the CFD mesh, up to the $j = 70$ spanwise section (rotating at a $\hat{M}_{tip} = 1.378$). (In the following, \hat{M}_{tip} will indicate the rotational Mach number of the outest spanwise mesh section, in order to distinguish it from M_{tip} , the actual *tip* Mach number of the rotating blade.) The rendering emphasizes the presence of a lateral surface S_l surrounding the blade and an end surface S_e formed by all sections of the inward grid layers at the same j index. The reported signature represents a converged solution. Although the very high time resolution adopted for the calculations (2048 time steps in a period, corresponding to an azimuthal step of 0.175°) the numerical signature exhibits a smooth behaviour. This result is not easy to achieve. It has been obtained through a preliminary spanwise refinement of the input grid and demonstrates the accuracy in the evaluation of the $\Sigma(t)$ function.

In order to prove the convergence of the numerical solution provided by the emission-porous surface formulation, extensive work has been carried out. Figure 6 shows six different noise predictions obtained by fixing the same $k = 35$ layer of the mesh, and progressively moving the spanwise boundary of the integration domain from the $j = 35$ section, close to the blade tip and rotating at a $\hat{M}_{tip} = 0.956$, up to the $j = 75$ section, corresponding to $\hat{M}_{tip} = 1.451$. The effects of the delocalization are clear. The contribution from sources placed outside the sonic cylinder is essential to obtain the expected asymmetrical shape of the noise signature. The resulting waveform

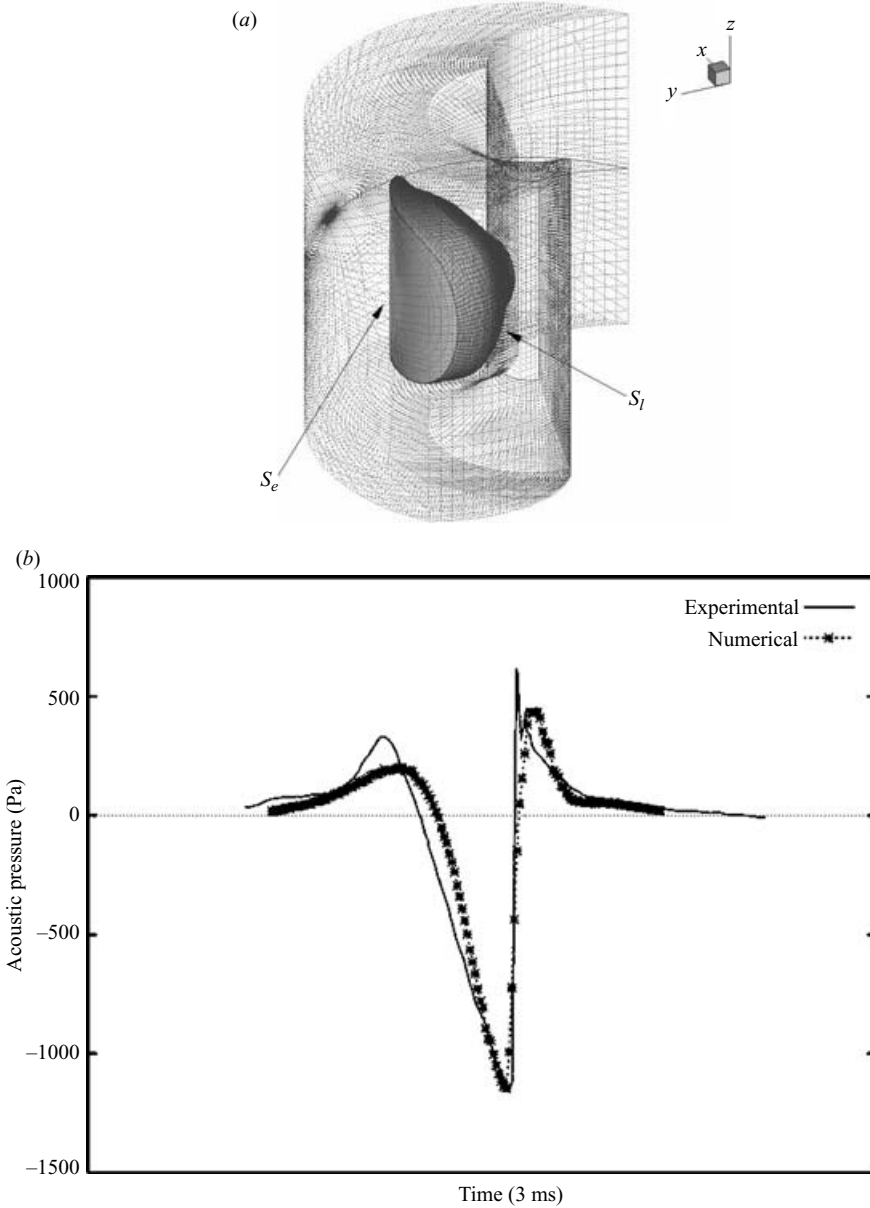


FIGURE 5. The comparison between the experimental data and the noise prediction provided by the emission-porous surface formulation for the UH-1H hovering rotor at $M_{tip} = 0.95$. (a) The rendered image of the adopted integration domain highlights the lateral (S_l) and end (S_e) surfaces.

corresponding to $\hat{M}_{tip} = 1.087$ (with the end surface S_e very close to the sonic cylinder) seems to match the recompression peak value very well, but overestimates the negative peak. It represents a not converged solution and the overestimation is due to the phase shift of the contributions from subsonic and supersonic sources (here not completely taken into account). This behaviour had already been noted through the use of the far-field approximation by Brentner (1997) and, in general, by the computations limited to the subsonic region. A converged solution is achieved at approximately $\hat{M}_{tip} = 1.3$.

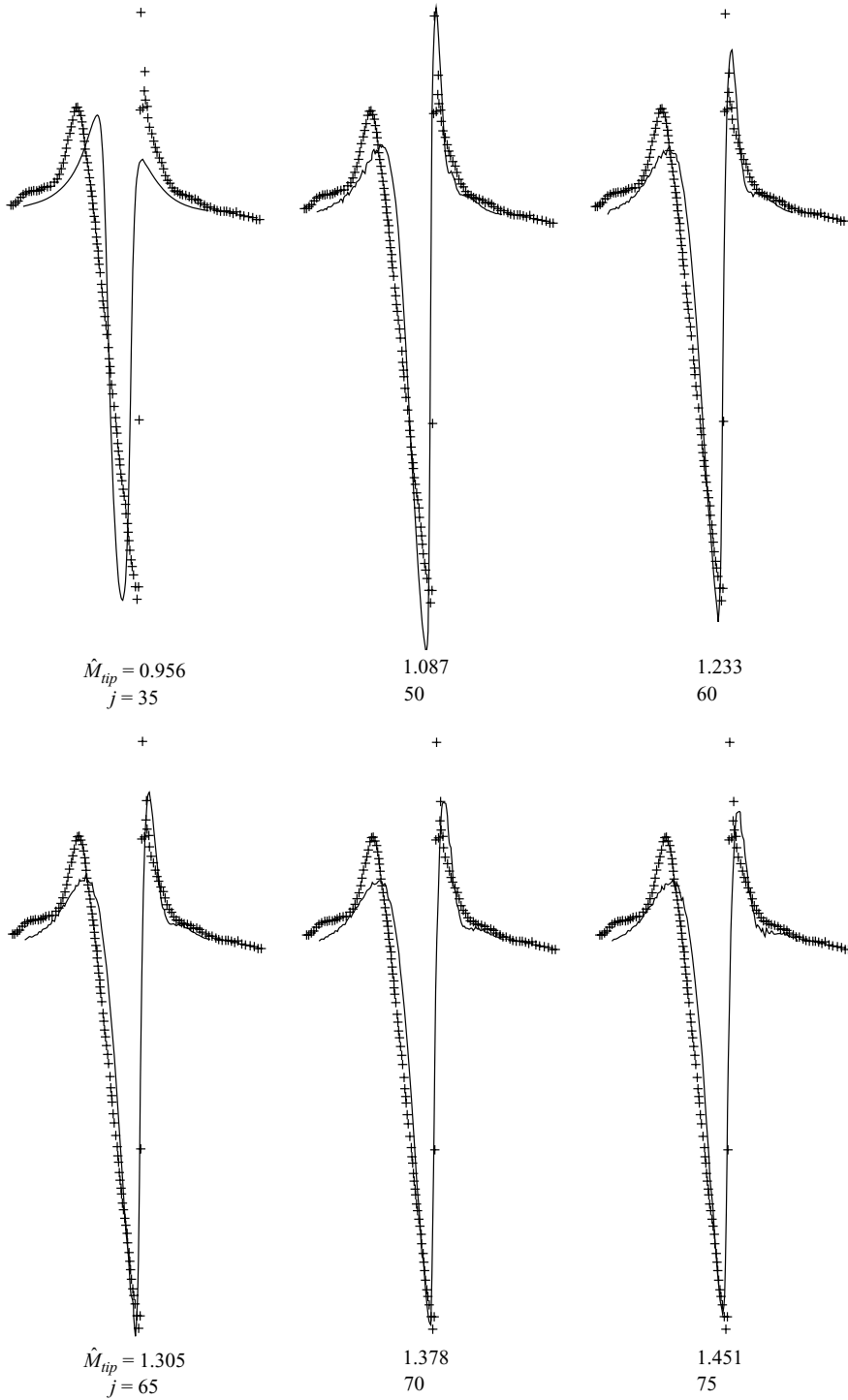


FIGURE 6. Convergence of the numerical noise predictions with respect to the spanwise extent of the integration domain. The markers represent the experimental data. The k layer of the CFD mesh is fixed to 35, as shown in figure 5(a).

For the convergence analysis (figure 7), where the control surface corresponds to subsequent layers of the grid limited to the $j = 70$ spanwise section (rotating at $\hat{M}_{tip} = 1.378$), because of the broadening and not uniform distribution of the spanwise sections on the different layers, a unique distance of the integration domain from the blade cannot be determined. Nevertheless, in order to estimate how far the S_p porous surface is from the body, we have considered the ratio

$$D_k = \frac{|\Delta x|_{tip}}{c},$$

where $|\Delta x|_{tip}$ represents the maximum chordwise extension of the k layer corresponding to the blade tip section and c is the blade chord. At $D_k = 1.0$, the control surface collapses on the blade and the noise prediction corresponds exactly to the sum of thickness and loading noise provided by formulation 1A. By moving away from the body, the resulting waveform is progressively affected by spurious fluctuations while the negative peak value moves towards the experimental data. This undesirable behaviour is due to the Λ singularity and will be treated in the next section. The converged solution is reported at $D_k = 14.8$ (corresponding to the $k = 30$ layer of the mesh). The most important result of this study is the unquestionable convergence of the numerical solution provided by the emission-porous surface formulation. Except for the spurious peaks caused by $\Lambda = 0$ singularity, all the noise predictions are physically correct and the convergence is related only to the contribution of supersonic sources actually taken into account in the calculations. Within the range $k = 26\text{--}40$ all the numerical predictions (not reported for brevity) do not exhibit any appreciable discrepancy.

4.1. The Λ singularity

In this section, we will focus our attention on the numerical behaviour of the Λ singularity of equation (2.9). This is an interesting and little-known issue. Different authors recognized the Λ term as a true logarithmic and non-integrable singularity which gives rise to infinite pulses in the computed noise waveforms. From a theoretical point of view, it is clear that such a singular behaviour does not have a physical meaning. It depends only on the adopted mathematical model. Farassat treated this problem extensively. He developed two different formulations (known as formulations 3 and 4) aimed at providing a numerical solution to the problem, but to my knowledge no result for a realistic configuration has ever been published. These formulations exhibit similar, but not equal, singular terms and express the contribution of the nonlinear terms as the sum of surface and line integrals. In particular, formulation 4 rewrites the double divergence of $T_{ij}H(f)$ in the fundamental equation (2.1) in order to extract some surface quadrupole terms and take the volume term back to the original form of the Lighthill equation. Intuitively, these surface quadrupole integrals have to remove the singular behaviour affecting the linear kernels. Again, the mathematical demonstration of this hypothesis has been provided by Farassat & Brentner (1998b), where all the singular terms of formulation 4 were proved to be integrable. Although formulation 4 is notably simpler than formulation 3, the complexity of these formulations make the development of prediction tools difficult. Then, our aim is to examine the numerical behaviour of the Λ singularity through a direct solution of equation (2.9) in order to explore the possibility of removing its effects in a more practical way.

4.1.1. Relations between Λ and Σ

Before starting the analysis of the Λ effects on noise predictions, let us focus our attention on the numerical condition $\Lambda = 0$ and its relation to the emission surface Σ .

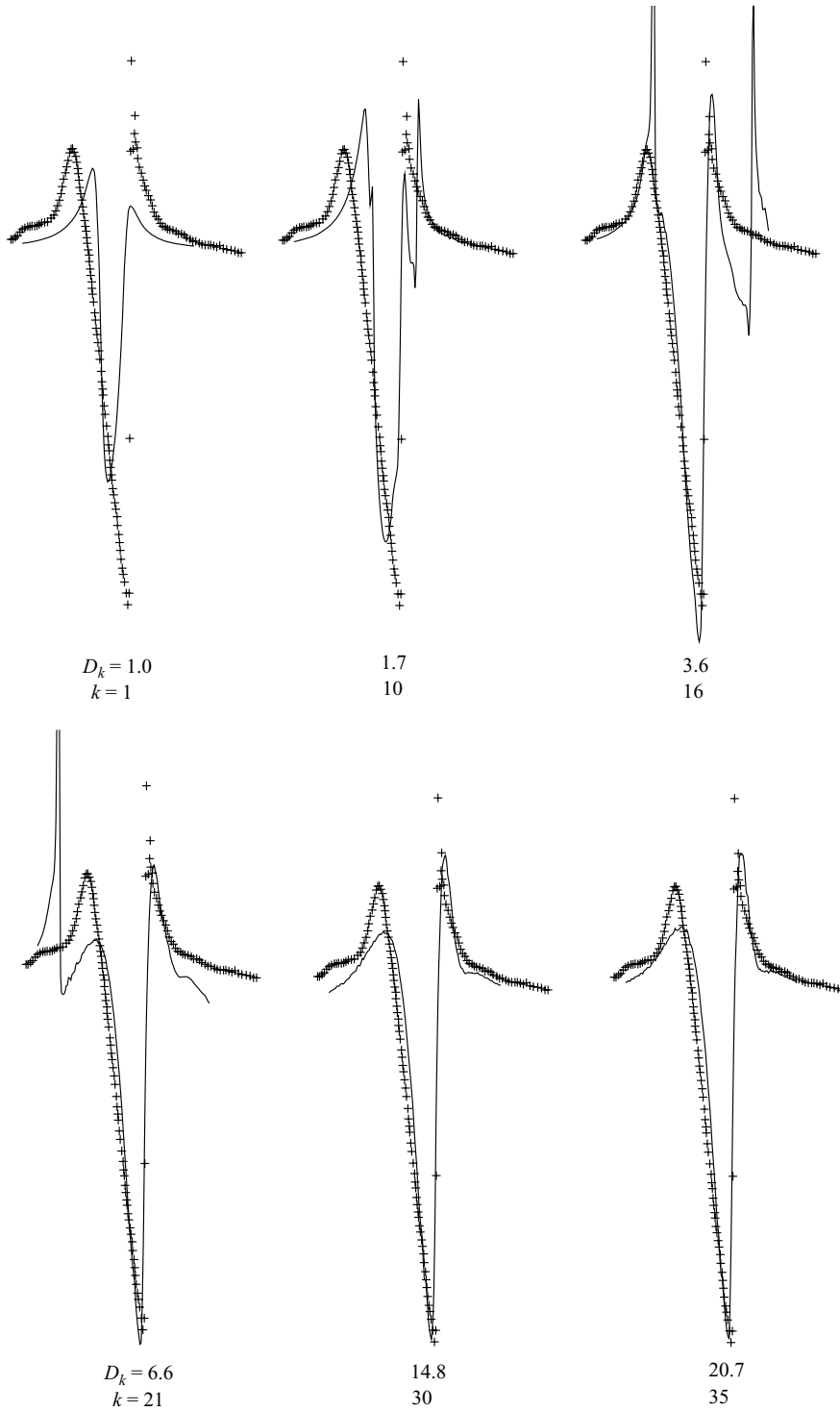


FIGURE 7. Convergence of the numerical prediction with respect to the outward extent of the integration domain. The spanwise boundary of the numerical mesh is fixed to $j = 70$, corresponding to a Mach number of 1.378.

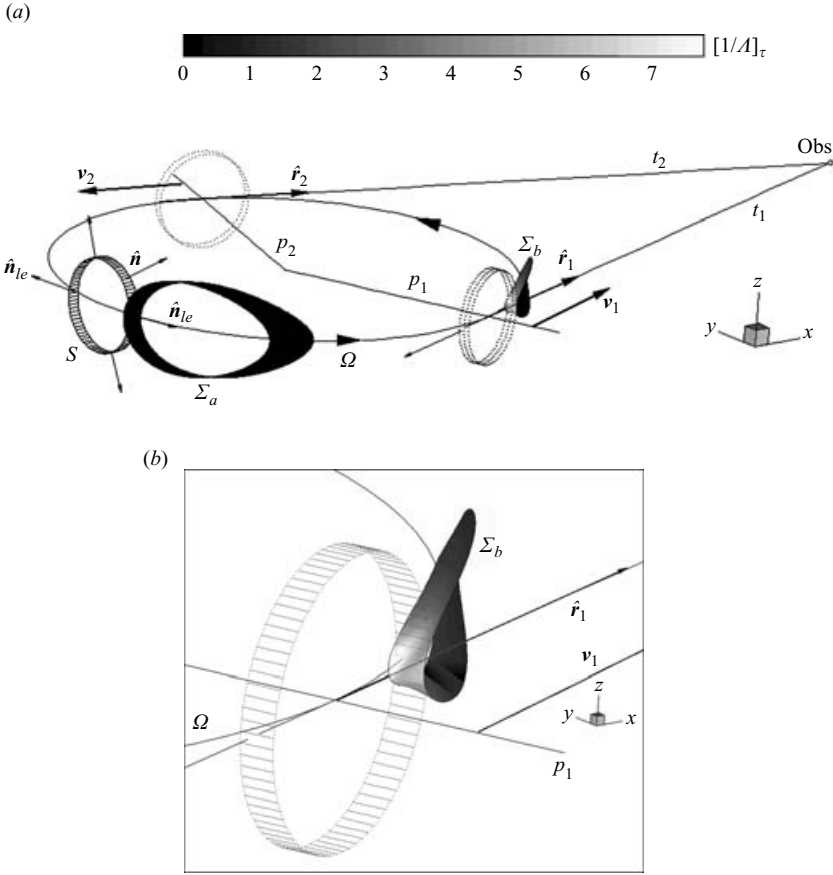


FIGURE 8. Three-dimensional view of a cylindrical strip S rotating at supersonic speed. (a) shows all the quantities concerning the evaluation of Δ and a critical configuration of the emission surface (here constituted by two unconnected domains Σ_a and Σ_b). The isocontours refer to the $[1/\Delta]_\tau$ maximum value determined on Σ . (b) An enlargement of the critical region where $[1/\Delta]_\tau$ tends to a high value.

Figure 8(a) depicts a simple strip of a cylindrical mesh with a circular cross-section named S (on the left-hand side in the figure). The strip is rotating along the circular trajectory Ω lying outside the sonic cylinder so that all the source points, generally corresponding to the centroids of the strip panels, rotate at supersonic speed. For clarity, the outward unit normal vector \hat{n} at different points on S is traced. In particular, the vectors \hat{n}_{le} and \hat{n}_{te} correspond to the strip leading and trailing edges, respectively. In the figure, t_1 and t_2 are the tangent lines to Ω passing through the in-plane observer, while p_1 and p_2 represent the radial directions perpendicular to t_1 and t_2 . The condition $\Delta=0$ occurs when M_n and the cross-product $\hat{n} \cdot \hat{r}$ have, simultaneously, an absolute value equal to 1 and the same sign, \hat{r} being the unit vector along the source-observer direction. Note that all these quantities must be determined at the emission time τ , but the unit normal vectors refer to S (not to Σ) so that the figure shows exactly the \hat{n} vectors which must be taken into account (at the appropriate azimuthal position) upon the emission surface. (In order to understand better the critical directions which the unit vector \hat{n} may assume on Σ , the strip S is traced with dotted lines at the azimuth angles corresponding to p_1 and p_2 .)

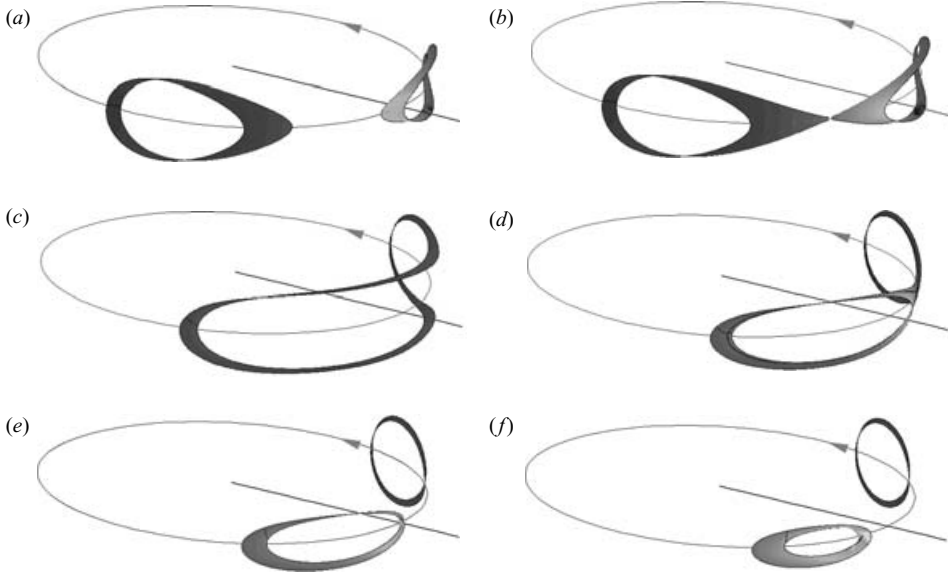


FIGURE 9. The time evolution of the emission surface subsequent to figure 8. (f) corresponds to a new critical configuration where some point on Σ approaches the $\Lambda = 0$ condition.

Intuitively, the figure points out that the only source points able to experience the alignment of the $\hat{\mathbf{n}}$ and $\hat{\mathbf{r}}$ vectors (with respect to the in-plane observer location) are the strip leading and trailing edges when approaching the critical lines p_1 and p_2 . In particular, depending on the strip rotational velocity, at p_1 the following conditions can occur:

$$\text{Leading edge: } M_n^{le} = \frac{\mathbf{v}_1 \cdot \hat{\mathbf{n}}_{le}}{c_0} = +1; \quad \hat{\mathbf{n}}_{le} \cdot \hat{\mathbf{r}}_1 = +1 \Rightarrow \Lambda = 0,$$

$$\text{Trailing edge: } M_n^{te} = \frac{\mathbf{v}_1 \cdot \hat{\mathbf{n}}_{te}}{c_0} = -1; \quad \hat{\mathbf{n}}_{te} \cdot \hat{\mathbf{r}}_1 = -1 \Rightarrow \Lambda = 0.$$

On the contrary, by approaching p_2 , no critical configuration of the emission surface can occur, since M_n and $\hat{\mathbf{n}} \cdot \hat{\mathbf{r}}$ always have opposite signs and Λ is always different from zero. Figure 8 shows a critical configuration of Σ corresponding to the cylindrical strip rotating at a Mach number of 1.1. The emission surface is constituted by two unconnected domains, named Σ_a and Σ_b , which approach each other. In particular, Σ_b widens up to intersect the critical line p_1 . At this stage of the emission surface time evolution Λ exhibits a sudden and notable decrease, which is qualitatively shown by the isocontours traced on the emission surface and representing the $[1/\Lambda]_\tau$ term of the integral kernels. The dangerous distribution of this term is highlighted in figure 8(b), where an enlargement of the critical region is shown. The subsequent time evolution of Σ can be appreciated in figure 9 where six different configurations of the emission surface are depicted. For clarity, these frames only show the trajectory Ω and the critical direction p_1 . It is evident that if no source point on the emission surface approaches the p_1 line (time steps a–d) the alignment of the $\hat{\mathbf{n}}$ and $\hat{\mathbf{r}}$ unit vectors cannot occur and the isocontours reveal a rather uniform, benign distribution of the $[1/\Lambda]_\tau$ term. On the other hand, at time steps e and f, a small region of Σ points at the observer along a direction close to the local outward normal; thus, Λ can experience a rapid decrease again. Qualitatively speaking, a change of the strip rotational velocity

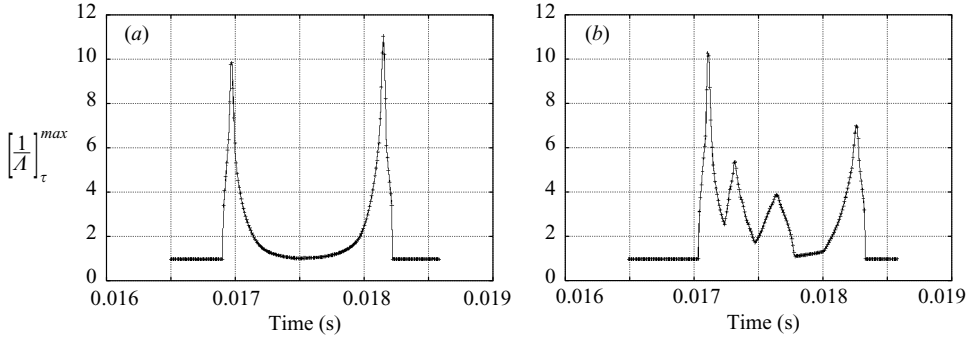


FIGURE 10. (a) The time history of the $[1/\Delta]_{\tau}^{max}$ maximum value determined on the emission surface corresponding to the circular strip of figure 8. (b) The same function refers to the clover section \tilde{S} depicted in figure 11.

(and, correspondingly, M_n) does not modify the main topological features of the emission surface shown in figure 9. Nevertheless, the critical configurations will occur at different azimuthal angles, so that the approaching of the critical direction p_1 can occur at the connection (figure 9b) or detachment (figure 9d) stage, or even at the early appearance of the Σ_b region in figure 8.

In order to appreciate better the behaviour of the Δ singularity within the revolution period, figure 10(a) shows the time history of the maximum value of the $[1/\Delta]_{\tau}$ term as determined on the emission surface corresponding to the circular strip. The presence of two cusp points suggests the undesirable consequences that this term can cause on the kernel functions of equations (2.3) and (2.9). It is worthnoting that the absolute value of Δ is never really close to zero. In fact, at each step, the mathematical condition $\Delta=0$ can be experienced by only one source point at one well-defined azimuthal angle. Therefore, even using a fine mesh and a limited time step, the occurrence of such a condition can be considered as a fortuitous case. The real numerical reason for the nearly infinite pulses appearing in the noise predictions is the general trend that Δ induces on the integral kernels and the requirement of computing a time derivative on such singular functions. The occurrence of peak values in the time history of the $[1/\Delta]_{\tau}$ term strongly depends on the observer location, the rotational speed and the shape of the surface S . Regarding this last aspect, we note that the circular section provides two cusp points because of the presence of a single critical direction p_1 . Nevertheless, this may not be the general case. Figure 10(b) shows a $[1/\Delta]_{\tau}$ time history exhibiting four singular points. It corresponds to the cross clover section \tilde{S} reported in figure 11 with the four critical configurations assumed by the corresponding emission surface. This shape is characterized by a concave region around the leading edge where different outward normal vectors may point towards the rotor plane. Thus, with respect to the in-plane observer, further possible directions for the alignment of the \hat{n} and \hat{r} can occur within the revolution period. Note the very complex topology assumed by the emission surface, constituted by two or three unconnected regions, and the different critical directions (out of the rotor plane at figures 10a and 10c, and in the rotor plane at figures 10b and 10d) highlighted through the isocontours of the $[1/\Delta]_{\tau}$ term.

From a qualitative point of view, accounting for a whole numerical mesh extended along span and surrounding the blade does not alter the relation between Δ and Σ . By considering a cylindrical mesh with a straight axis and a uniform spanwise

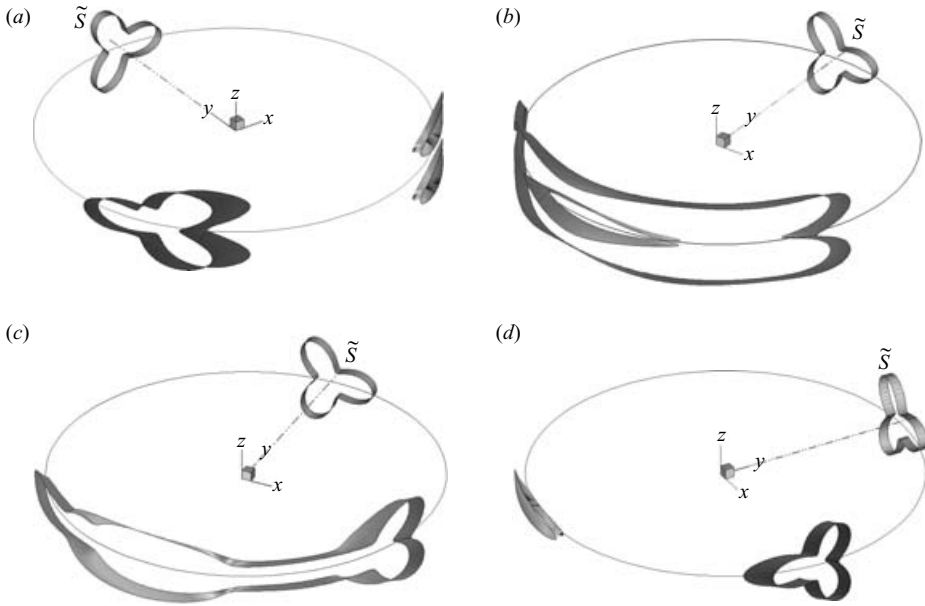


FIGURE 11. The four critical configurations assumed by the emission surface of the *clover* strip rotating at $M_{tip} = 1.1$. For clarity, the original section shape is shown within each frame, at the azimuth reference position $\psi = 0$. These configurations correspond to the four cusp points of the $\max[1/\Lambda]_\tau$ time history in figure 10(b).

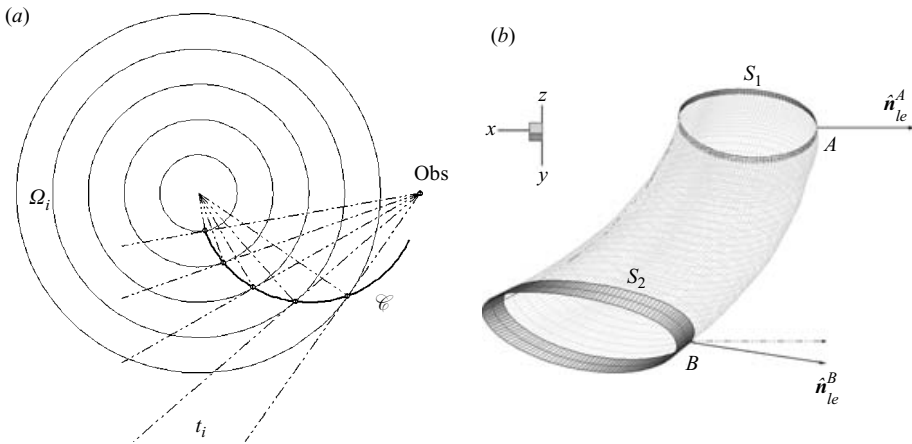


FIGURE 12. (a) The critical curve \mathcal{C} representing the envelope of the intersection points between the trajectories Ω_i and the corresponding tangent lines t_i passing through the observer location. (b) The mutual position of the outward normal vector at points A and B on a sweptback tip mesh is shown.

distribution of a circular section, it is possible to identify a *critical curve* \mathcal{C} . It represents the envelope of the intersection points between the tangent lines t_i to the trajectories Ω_i and the corresponding radial directions p_i (figure 12a). At these conditions, the singular behaviour of the acoustic integrals arises when the emission surface approaches the curve \mathcal{C} . Nevertheless, such a numerical mesh does not represent the best choice for noise predictions. For instance, figure 12(b) shows a portion of the

$k = 15$ layer of the Euler mesh used in the paper. The requirement of capturing the delocalized shock waves urges the adoption of a sweptback mesh outside the sonic cylinder. The behaviour of the inner elliptic section S_1 (with the leading edge A and the corresponding outward normal vector $\hat{\mathbf{n}}_{le}^A$) is very similar to the circular shape depicted in figure 8, but the normal vector $\hat{\mathbf{n}}_{le}^B$ at the leading edge B of the outer section S_2 is rotated with respect to $\hat{\mathbf{n}}_{le}^A$. Then, the normal vector $\hat{\mathbf{n}}_{le}^B$ will experience the possible alignment with the source observer direction at an azimuthal angle greater than at point A . This means that the critical curve \mathcal{C} generally differs from the curve depicted in figure 12(a) and depends on both the observer location and the local shape of the mesh.

These results show some interesting features of the Λ singularity and provide useful information about the numerical solution of equation (2.9), where the integration domain S_p can be chosen in an arbitrary way. It is clear that the Λ singularity may affect the noise prediction with spurious fluctuations and an unsuitable choice of the porous surface can even amplify such undesirable effects. On the other hand, the visualization of the emission surface and the knowledge of the Λ behaviour enable the recognition of which time steps are affected by the singularity and can give a useful indication about the reliability of the resulting noise predictions. Even better, a suitable choice of the porous surface allows us to move the insidious cusp points of the $[1/\Lambda]_\tau$ term far from the negative peak value of the acoustic pressure.

4.1.2. Effects of Λ singularity on noise prediction

This section is devoted to the analysis of Λ effects on the evaluation of the acoustic pressure time history for the UH-1H hovering blade at $M_{tip} = 0.95$. To this aim, we will first consider an integration domain corresponding to the $k = 15$ layer of the Euler mesh (up to $j = 70$). Note that such a control surface does not provide a converged solution and is here considered merely to point out some fundamental features of the numerical solution. The time range of calculations has been extended in order to cover half a revolution period.

Figure 13 shows the computed noise signatures; in particular, both the pseudothickness and pseudoloading components are reported, with the comparison between the overall noise prediction and the experimental data. Two nearly infinite pulses affect the pressure time histories of both the linear components at approximately $t_{\Lambda_1} = 0.020029$ and $t_{\Lambda_2} = 0.020783$. Nevertheless, the singular behaviour for the thickness and loading noise terms is of opposite sign so that, in the overall signature, their effect is somewhat mitigated with respect to the single components. Actually, a mutual opposition between the pseudolinear terms seems to characterize the different waveforms within the whole range of calculation except the narrow time region corresponding to the peak value of the experimental data (taking place at $t_p = 0.020386$). The most prominent feature of the resulting signature is the appearance of two spurious fluctuations at the critical time steps t_{Λ_1} and t_{Λ_2} . In order to prove that this behaviour is due to the Λ singularity, figure 14(a) shows the time history of the $[1/\Lambda]_\tau$ maximum value determined on the emission surface and figure 14(b) shows the following kernel functions

$$\mathcal{J}_1 = \int_{\Sigma} \left[\frac{1}{\Lambda} \right]_{\tau} d\Sigma, \quad \mathcal{J}_2 = \int_{\Sigma} \left[\frac{\rho U_n}{r} \right]_{\tau} d\Sigma, \quad \mathcal{J}_3 = \frac{1}{c_0} \int_{\Sigma} \left[\frac{L_r}{r} \right]_{\tau} d\Sigma. \quad (4.1)$$

As expected, the cusp points occurring in the time history of $[1/\Lambda]_\tau$ exactly correspond to the singular behaviour of the \mathcal{J}_1 term, while \mathcal{J}_2 and \mathcal{J}_3 do not exhibit any relevant feature at the critical time steps t_{Λ_1} and t_{Λ_2} . Because of the elliptic shape of

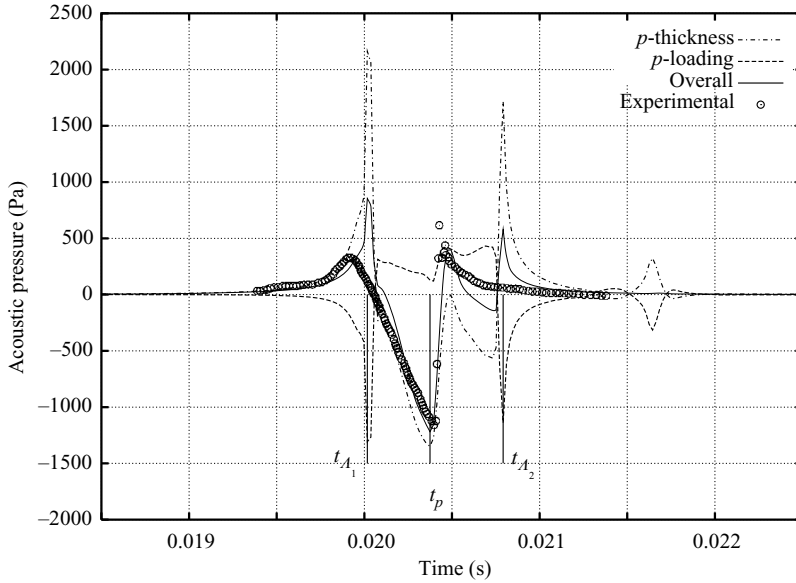


FIGURE 13. The noise signature obtained by using the $k=15$ mesh layer, split into the pseudothickness and pseudoloading components and compared with the experimental data. Note the spurious peaks due to Λ and the resulting fluctuations affecting the overall noise prediction at t_{A_1} and t_{A_2} .

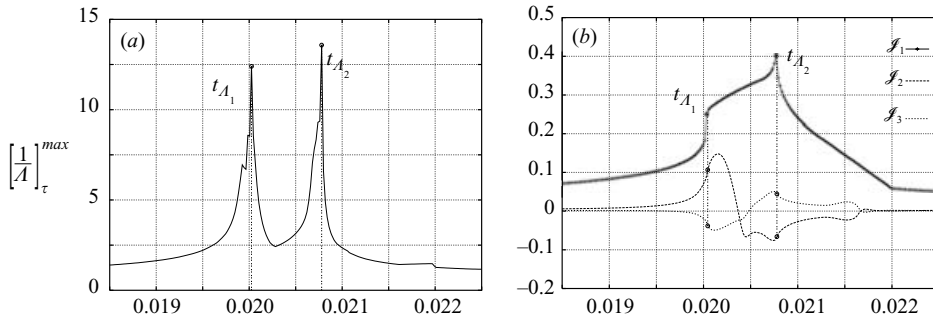


FIGURE 14. (a) The time histories of the $[1/\Lambda]_{\tau}$ maximum value and (b) the kernel functions defined in (4.1), corresponding to the noise signature reported in figure 13.

the mesh cross-section and the in-plane observer location, these two steps correspond to the approach of the emission surface to a critical curve \mathcal{C} lying in the rotor plane.

In particular, the time range around t_{A_1} concerns the early effects of multi-emissive sources. In fact, the first $[1/\Lambda]_{\tau}$ cusp point corresponds to the occurrence of unconnected patches which immediately appear being located along a well-defined direction. A sketch of such a configuration is shown in figure 15. The rendered image (figure 15a) shows the complex shape of the emission surface while the isocountours of the $[1/\Lambda]_{\tau}$ term (figure 15b) highlight the alignment of the unconnected regions along the hidden \mathcal{C} curve. The zoom pictures highlight the fragmented critical regions determined by the algorithm. Very soon, these fragments link together and form a single manifold which widens and moves away from the critical curve. Figure 16 shows the Σ surface at t_p , where the negative peak value of the acoustic pressure takes

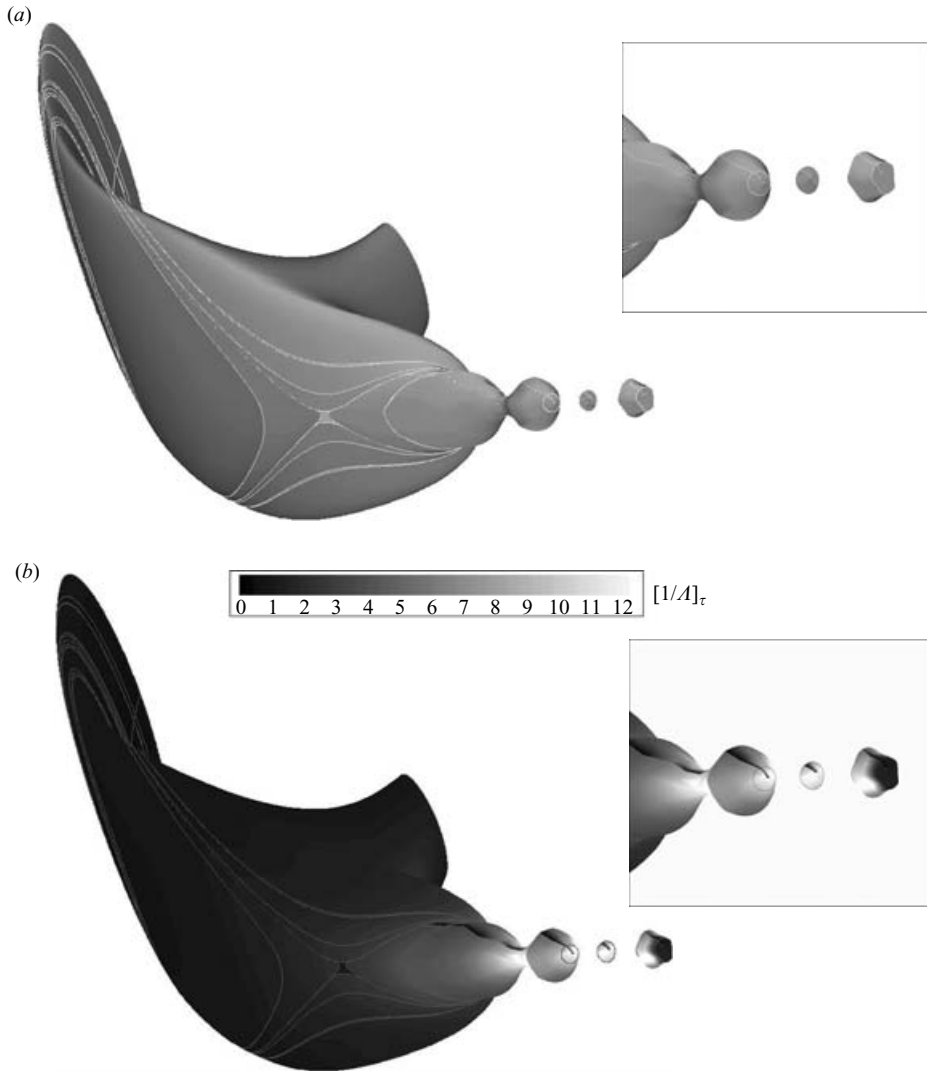


FIGURE 15. The Σ surface at a time step very close to t_{A_1} exhibits a notable fragmentation. The $[1/\Lambda]_\tau$ isocontours reveal the alignment of the unconnected patches along a well-defined direction, which represents the critical curve \mathcal{C} of the problem. The zoom pictures highlight the fragmented, critical regions as modelled by the algorithm.

place. The isocontours reveal a uniform distribution of the dangerous $[1/\Lambda]_\tau$ term and confirm the reliability of the noise prediction (matching rather well the experimental data) at such an important stage. The second nearly infinite pulse occurring at t_{A_2} is due to the approach to the critical curve by the trailing edge of the emission surface and its tendency to separate into two different domains. This is a critical stage, since the separation takes place through a continuous shrinking of a linking strip which finally disappears after forming a cusp-edge. Such a configuration is described by Farassat & Brentner (1998*b*), where the authors stated that the condition $\Lambda = 0$ is equivalent to the emission surface becoming pointed. Figure 17 shows this detachment stage with the occurrence of an irregular cusp-edge still partially linking the two regions. Again, the isocontours reveal clearly the exact location of the critical curve. Finally, while

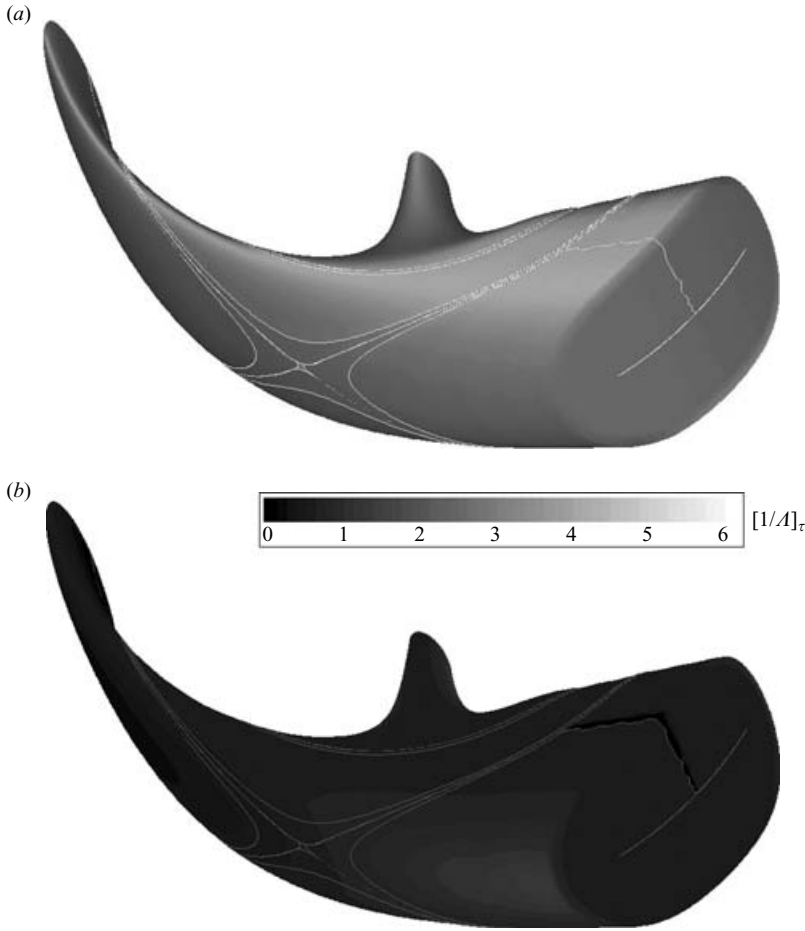


FIGURE 16. At $t = t_p$, when the negative peak of the acoustic pressure takes place, the Σ surface appears as an extended and single manifold with a uniform distribution of the $[1/\Delta]_\tau$ term. As mentioned in §2, the curves appearing on Σ represent the boundaries of the different patches determined by the algorithm (see the Appendix).

the region linked to the subsonic branch goes on rotating, the other one progressively reduces: when all the source points come back to a single-emissive status, this region disappears.

From a numerical standpoint, it is worthnoting that the occurrence and the collapse of unconnected regions do not affect the noise prediction at all. This is exactly what we expect, since the physical phenomenon proceeds in a continuous way and the resulting noise signature must not suffer the possible instabilities related to the numerical model.

Actually, the computation of the integral terms (usually achieved through a simple zero-order formulation) requires the evaluation of the area of each panel even though the number of the $\mathbf{y}(\tau)$ retarded locations reduces to a handful of points. Furthermore, the identification of the different patches always concerns a discrete domain and strongly depends on the distribution of spanwise and chordwise sources.

Thus, when only a few points experience a multi-emissive status (as around t_{A_1}) or when a critical configuration with a cusp-edge or a hole appears (as around t_{A_2}), some instability of a numerical nature seems to be inevitable. This problem may become

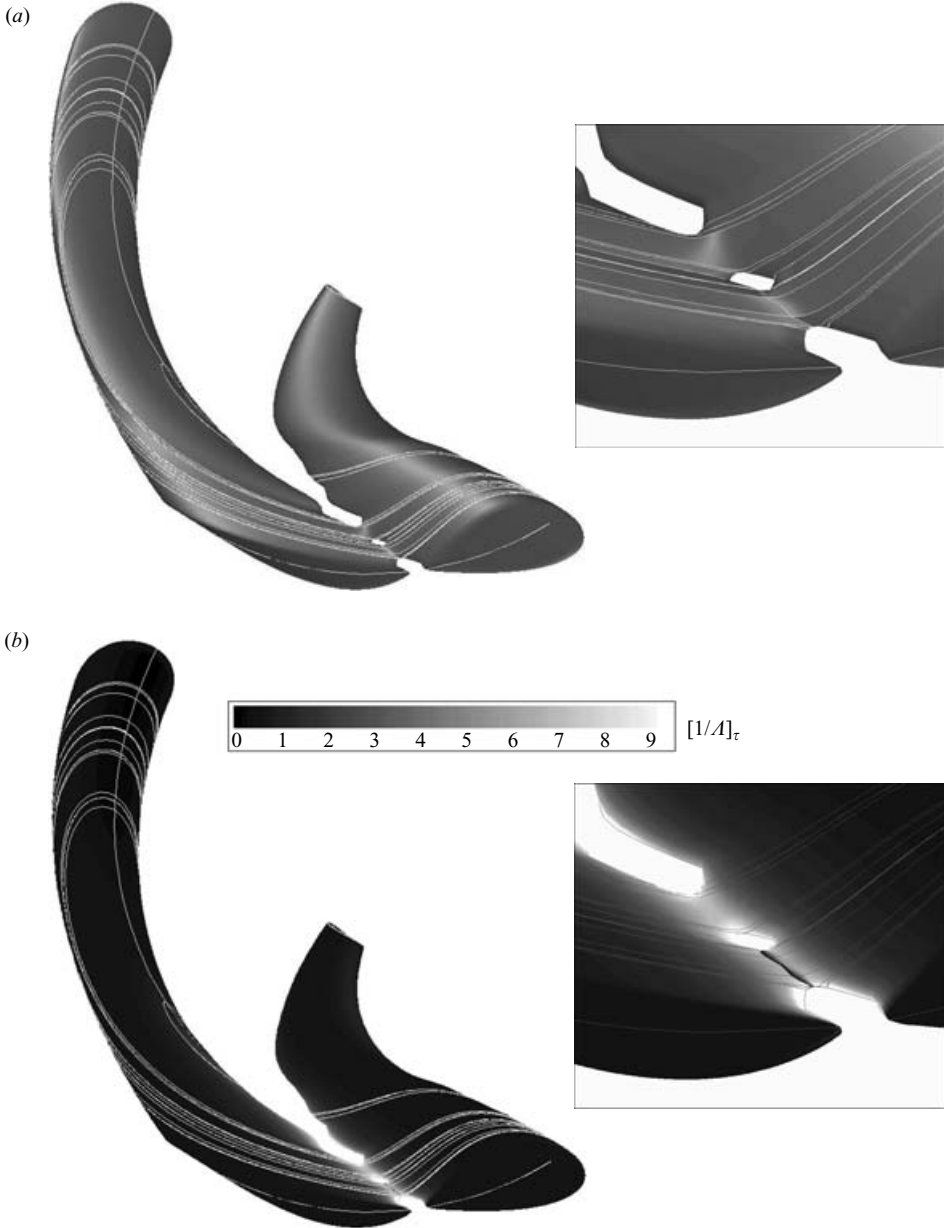


FIGURE 17. Approaching the time step t_{A_2} the emission surface tends to separate into two different domains. The separation strip shrinks up to form an irregular cusp-edge which is clearly shown in the zoom pictures. Again, the $[1/\Delta]_{\tau}$ isocontours highlight the position of the critical curve.

relevant by diminishing the time step of calculation and can be only partially solved through the use of a finer mesh. Nonetheless, all the noise predictions reported in this paper and obtained with a high time resolution exhibit a smooth waveform. These results confirm (Wells 1991) that the smoothness of the noise predictions is not related to the time derivative outside the integral terms and depends only on the accuracy and robustness of the algorithm devoted to modelling of the emission surface. The

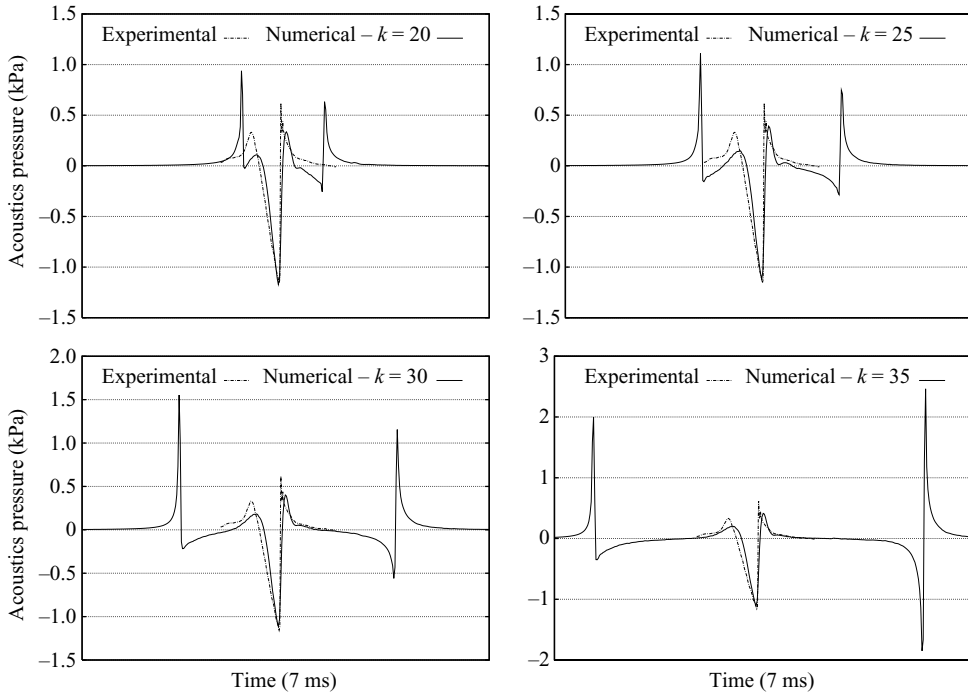


FIGURE 18. Broadening of the control surface, which corresponds to subsequent k layers of the CFD mesh, causes the increase of the distance between the critical time step t_{A_1} and t_{A_2} and the nearly infinite pulses due to the Λ singularity.

comparison between the overall signature and the experimental data in figure 13 proves that the Λ singularity can notably affect the resulting noise prediction. In this case, it gives rise to fictitious pressure fluctuations which are not easily recognizable and are not physically related to the noise emission phenomenon. Nevertheless, such a comparison refers to an integration domain rather close to the blade, which does not provide a converged solution.

At this stage, by moving the control surface away from the blade, a double purpose can be pursued. First of all, the contribution from all the nonlinear terms is taken into account thus obtaining a converged solution; but the most interesting aspect concerns the Λ singularity effects. Accounting for a wider integration domain corresponds to increasing distance between the leading and trailing edges of the porous surface S_p . The cusp points of the $[1/\Lambda]_\tau$ term are related to the crossing of the critical curve by the emission surface. As shown in the previous section, this crossing is directly related to the S_p leading and trailing edges. Thus, the enlargement of such a domain causes a shift between the critical steps t_{A_1} and t_{A_2} on the time axis. In particular, the wider the integration domain, the larger the time shift. Then, owing to the numerical nature of the Λ singularity, the choice of a wide control surface should enable the recognition and isolation of the fictitious pressure fluctuations from the actual noise signature. This assumption is confirmed by the numerical results. Figure 18 shows four different noise predictions obtained by assuming the $k=20, 25$ and 35 layers of the CFD mesh as integration domain. As expected, the numerical solution rapidly converges towards the experimental data while the spurious pulses due to Λ move away from the acoustic pressure waveform. Note that the best numerical result corresponds to

the outer layer ($k = 35$) of the mesh: it provides a fully converged solution and the nearly infinite pulses are so far from the acoustic pressure negative peak that they could be artificially removed.

4.2. What is a supersonic thickness noise?

The evaluation of the integral terms of the FW-H equation for a blade rotating at supersonic speed represents a challenging problem. The numerical manipulation of these terms can provide unexpected results and lead to some questionable conclusions. This is probably because the solution of equation (2.1) is usually thought of (and searched for) as the sum of different contributions (thickness, loading and quadrupole noise), but such a subdivision can be misleading at supersonic speed. Amiet (1988) and Wells (1988) focused attention on the monopole term of an infinitely thin blade. The noise signatures were determined through the so called *acoustic planform method*, where the three-dimensional Σ domain was reduced to a flat emission surface corresponding to the blade planform. Amiet was the first to achieve very smooth noise predictions for a biconvex blade at supersonic speed ($M_{tip} = 1.1$). He showed the effects of a sweptback blade tip on the acoustic pressure waveforms. All the same, the noise signatures were characterized by the presence of anomalous and abrupt slope changes; Amiet correctly identified the acoustic planform configurations corresponding to these singular points, but concluded by hoping for a better understanding of their own nature. Wells revisited Amiet's results by accounting for more complex blade shapes. She discussed the mathematical nature of the singularities and correctly related the occurrence of the slope changes in the acoustic pressure waveform to the time derivative of the $\Sigma(t)$ function.

All these papers, however, assume the monopole contribution at supersonic speed as being a part of the acoustic pressure field, thus associating it to a definite physical meaning. The use of the emission-porous surface formulation suggests an alternative point of view, where the integral term corresponding to the usual thickness noise component does not represent an actual *noise* signature. In order to clarify this last assertion a cylindrical porous surface S_A , nearly attached to the blade and with a biconvex cross-section has been taken into account. This surface allows a qualitative comparison with the results published by Amiet and highlights some numerical aspects of the problem. Through a trilinear interpolation procedure, the aerodynamic data on S_A have been extracted from the CFD mesh of the UH-1H hovering rotor at $M_{tip} = 0.95$. Then, some different spanwise extensions of the mesh were accounted for in order to obtain an increased tip Mach number of the integration domain. (Note that the increased tip Mach number can be obtained by increasing the blade rotational velocity ω , but this value is intentionally not changed in order to retain the same operating conditions. This should better explain the fact that the overall noise prediction (figure 19) does not change and, therefore, the notable differences occurring in the monopole term waveforms at different M_{tip} (figure 22) are reasonably of numerical (not physical) nature.) A sketch of S_A is depicted in figure 19, at the top. The three-dimensional view emphasizes the straight spanwise shape of the control surface with respect to the sweptback tip shape of the first CFD mesh layer (partially corresponding to the blade). At the same time, the side view gives an idea of the very small distance separating the blade from S_A . Figure 19(b) shows the comparison between the overall noise prediction as provided by formulation 1A (with the integration domain limited to the blade surface) and equation (2.9) through the use of S_A at different tip Mach numbers. As expected, the difference is very small.

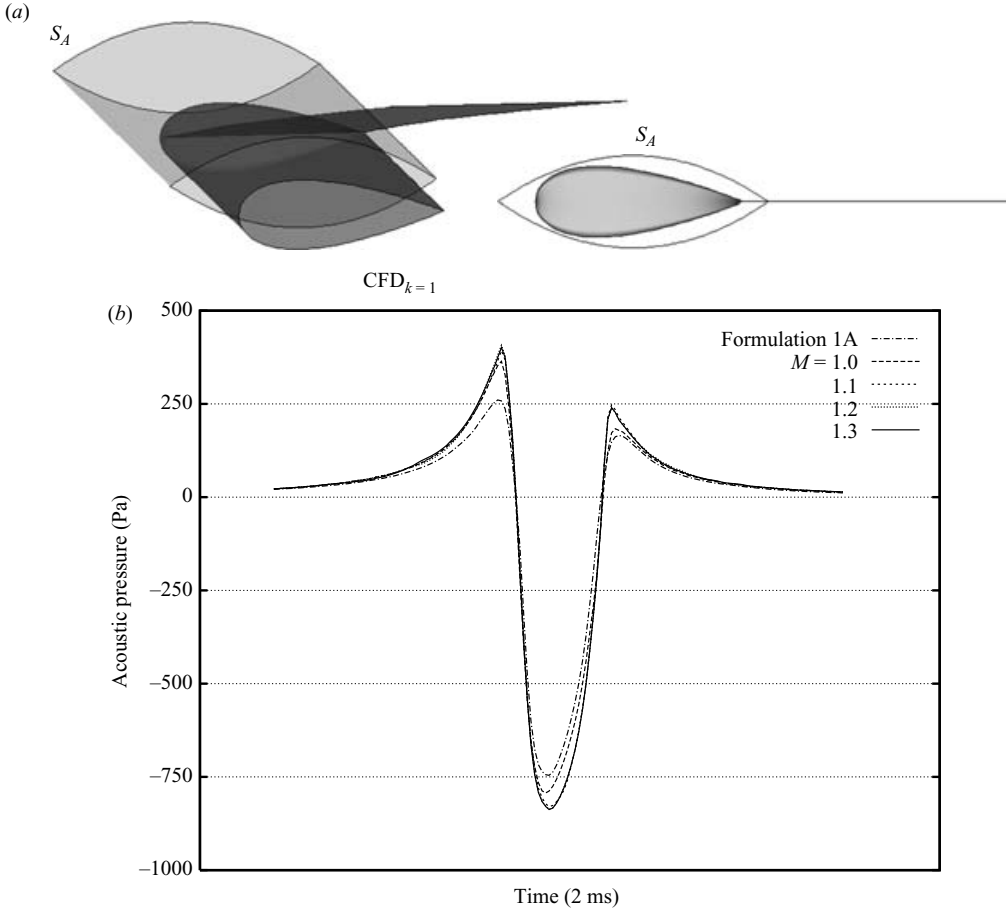


FIGURE 19. (a) A three-dimensional and side view of the porous surface S_A used to qualitatively reproduce the Amiet results are sketched. (b) A comparison between the noise prediction provided by formulation 1A and the emission-porous surface formulation by using four different spanwise extents of S_A (corresponding to a tip mesh section rotating at a Mach number from 1.0 to 1.3).

The physical meaning of this difference is clear: it represents the contribution from the delocalized noise sources placed in the limited region between the body and the control surface and outside the blade tip. Beyond a porous surface tip Mach number of 1.1, the computational solution is converged. In fact, the main contribution of the delocalized sources follows the sweptback shape of the CFD mesh outside the sonic cylinder, so that a further extension of S_A along the radial (span) direction, corresponding to a higher tip Mach number, does not change the noise prediction.

At this stage, the signatures of figure 19(b) can be broken up into different contributions. Let us focus the attention on the monopole term. Because of the definition of the U_i operator of (2.6), the pseudothickness component p_T can be split into the following integrals

$$\begin{aligned}
 4\pi p_T(\mathbf{x}, t) &= \frac{\partial}{\partial t} \int_{\Sigma_p} \left[\frac{\rho_0 v_n}{r\Lambda} \right]_{\tau} d\Sigma_p - \frac{\partial}{\partial t} \int_{\Sigma_p} \left[\frac{\rho v_n}{r\Lambda} \right]_{\tau} d\Sigma_p + \frac{\partial}{\partial t} \int_{\Sigma_p} \left[\frac{\rho u_n}{r\Lambda} \right]_{\tau} d\Sigma_p \\
 &= \mathcal{F}_1 + \mathcal{F}_2 + \mathcal{F}_3.
 \end{aligned} \tag{4.2}$$

The first term \mathcal{T}_1 represents the well-known thickness noise contribution of the linear formula referred to the porous surface S_A understood as a rigid body. Numerically speaking, it corresponds exactly to the noise term determined by Amiet and claimed as a supersonic thickness noise signature. As usual, this term depends only on geometrical and kinematic quantities. On the contrary, the \mathcal{T}_2 and \mathcal{T}_3 integrals are related to the density and velocity three-dimensional distributions upon the integration domain placed far from the body. Thus, they can be considered as field terms since they introduce in the numerical solution the effects of the aerodynamic field quantities. By using a porous surface S_A with an outer spanwise section rotating at $\hat{M}_{tip} = 1.1$, the evaluation of the different integral terms in (4.2) provides the waveforms depicted in figure 20. Note that, because of the notable impulsive nature of the noise signature at such a supersonic speed, the numerical predictions have been determined with a high time resolution (4096 steps per period), corresponding to an azimuthal step of approximately 0.088° . As expected, the \mathcal{T}_1 time history reported in the top figure matches very well the analogous noise prediction achieved by Amiet (1988). The signature is characterized by two singular points, S_1 and S_2 , and four discontinuity points θ corresponding to an abrupt slope change of the pressure waveform. Nevertheless, this integral term is numerically balanced by the \mathcal{T}_2 field term and just the sum of $\mathcal{T}_1 + \mathcal{T}_2$ (which is not zero) with the last term \mathcal{T}_3 provides the reasonable (and expected) pseudothickness noise signature p_T reported figure 20(b). The main features of the \mathcal{T}_1 waveform are very different from the resulting p_T component. It does not exhibit any trace of both discontinuity and singular points. The \mathcal{T}_1 integral contribution seems to have no physical meaning on its own. We are conscious that these results refer to a blade rotating at a tip Mach number equal to 0.95, not to 1.1. Furthermore, when the S_A control surface collapses upon the body, the impermeability condition imposes a mutual cancellation between \mathcal{T}_2 and \mathcal{T}_3 , while the \mathcal{T}_1 contribution still represents a part of the solution. In this case, however, the beneficial effect of \mathcal{T}_2 on \mathcal{T}_1 should be replaced by some other field contribution (from the quadrupole term, as indicated by formulation 4) in order to provide a reasonable noise prediction. On the other hand, if an actual supersonic tip speed blade were taken into account, the use of the emission-porous surface formulation should provide exactly the same \mathcal{T}_1 term, and a different behaviour could concern merely the field terms \mathcal{T}_2 and \mathcal{T}_3 (because of the different density and velocity fields). These results suggest that the \mathcal{T}_1 term does not represent the thickness noise from a supersonic tip speed blade; it is probably not a noise signature at all.

The characteristic θ points termed by Amiet as ‘near-singularities’ correspond to four special configurations of the emission surface. In particular, the time steps t_{θ_1} and t_{θ_4} concern the appearance and disappearance, respectively, of multiple emission times and, consequently, of an unconnected region within the Σ domain. On the contrary, the steps t_{θ_2} and t_{θ_3} correspond to a topology change of the retarded manifold, whose tip section turns from a multiconnected to a single shape and vice versa. A sketch of these critical steps is shown in figure 21 for the control surface S_A rotating at a tip Mach number of 1.1. As noted by Wells & Han (1993), the critical time steps correspond to non-singular discontinuities in the time derivative of the $\Sigma(t)$ function and are responsible for the Amiet near-singular points.

An increase of the rotational velocity does not alter the essential features of the Σ surface time evolution, even though the critical configurations occur at different time steps. Figure 22 shows a qualitative comparison of the \mathcal{T}_1 and \mathcal{T}_2 time histories at different Mach numbers. As expected, a higher value of the Mach number brings forward θ_1 and θ_2 and postpones θ_3 and θ_4 along the time axis. For clarity, figure 23(a)

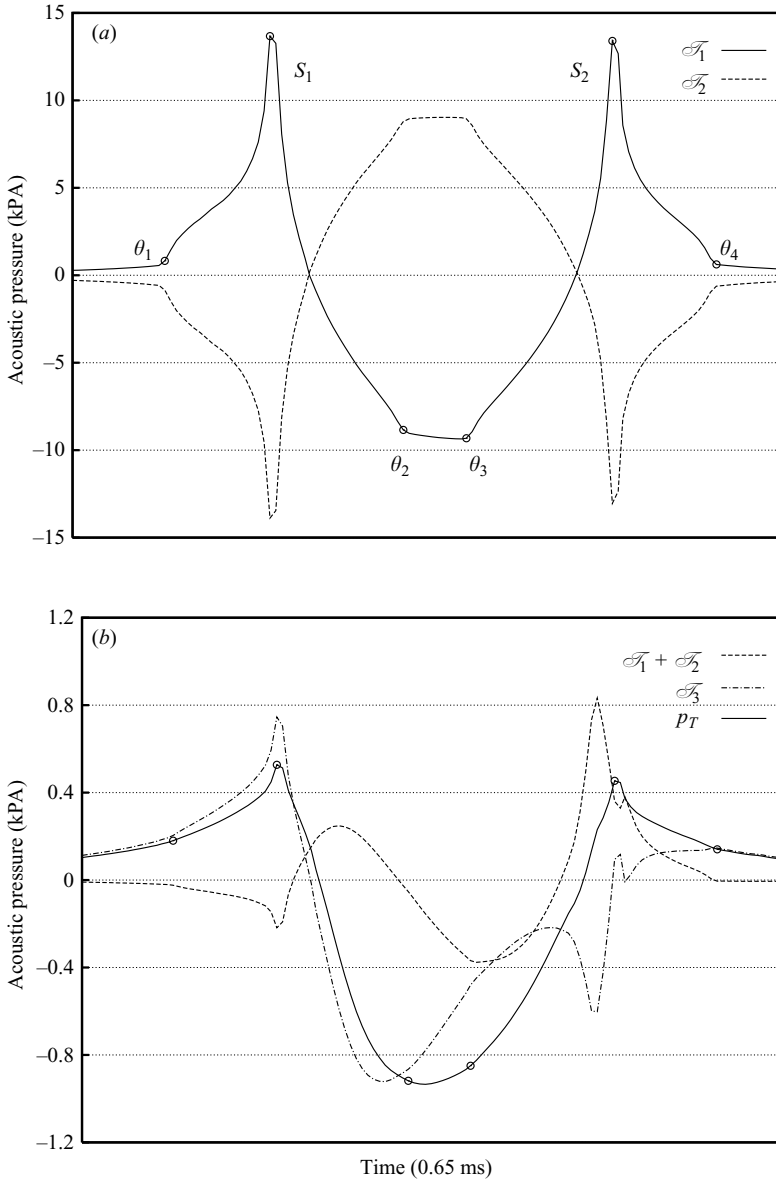


FIGURE 20. (a) The time histories of the \mathcal{T}_1 and \mathcal{T}_2 integral terms for the biconvex S_A control surfaces rotating at $\hat{M}_{tip} = 1.1$. (b) The sum of these terms, the \mathcal{T}_3 component and the overall pseudothickness noise component.

shows the critical Σ configurations corresponding to the cited change of topology (steps t_{θ_2} and t_{θ_3}) for the control surface rotating at $\hat{M}_{tip} = 1.3$. Even though these configurations concern an unconnected region of the Σ surface, there is no qualitative difference with respect to the previous case. The contribution from the \mathcal{T}_2 integral term still removes the discontinuity points affecting the \mathcal{T}_1 signature from the overall pressure waveforms. Figure 23(b) shows the time derivatives of the $\Sigma(t)$ functions determined at a tip Mach number of 1.1 and 1.3. By increasing the rotational velocity, the θ points move along the time axis and the curve exhibits the same numerical

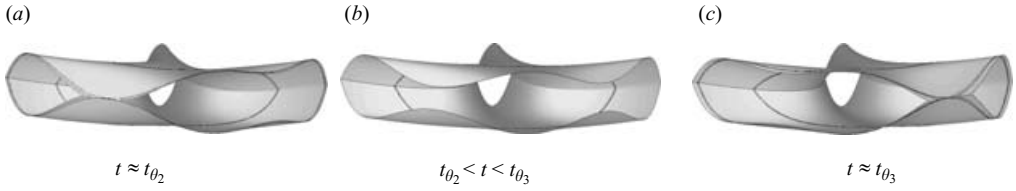


FIGURE 21. The critical time steps t_{θ_2} and t_{θ_3} correspond to a change of topology of the Σ surface, where the tip section turns from (a) a multiconnected shape to (b) a single curve and (c) vice versa.

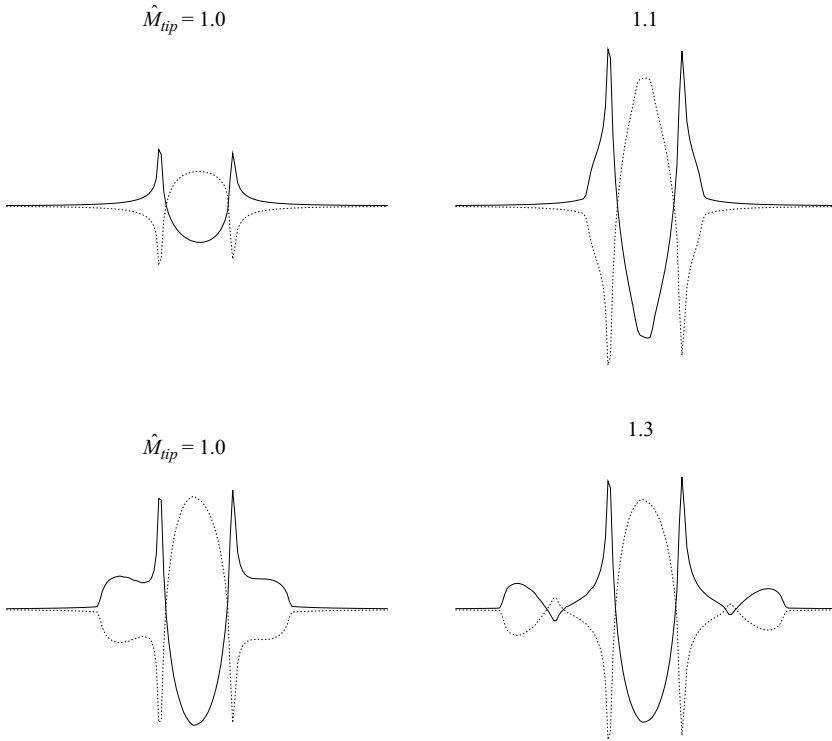


FIGURE 22. By increasing the rotational velocity the near-singular points affecting the \mathcal{T}_1 (solid lines) and \mathcal{T}_2 (dotted line) time histories move along the time axis. Nevertheless, the sum of these two terms always provide a mutual cancellation of such fictitious features of the resulting noise signature, so that the overall pressure waveforms (figure 19b) do not change.

behaviour of the integral terms waveforms. All the signatures depicted in figure 22 represent a part of the numerical solutions shown in figure 19 which do not exhibit any slope changes and, above all, are not altered by the increased tip Mach number. Therefore, rather than an acoustic pressure time history, the \mathcal{T}_1 waveform somehow appears as a *filtered representation* of the Σ surface time evolution.

It is worth noting the similarity between the numerical results reported in figure 22 and figure 18, where the choice of a wider porous surface could suitably shift the singular peaks owing to the Λ singularity. Here, the use of a spanwise enlarged domain can shift the near-singular points owing to the Σ time derivative, but in

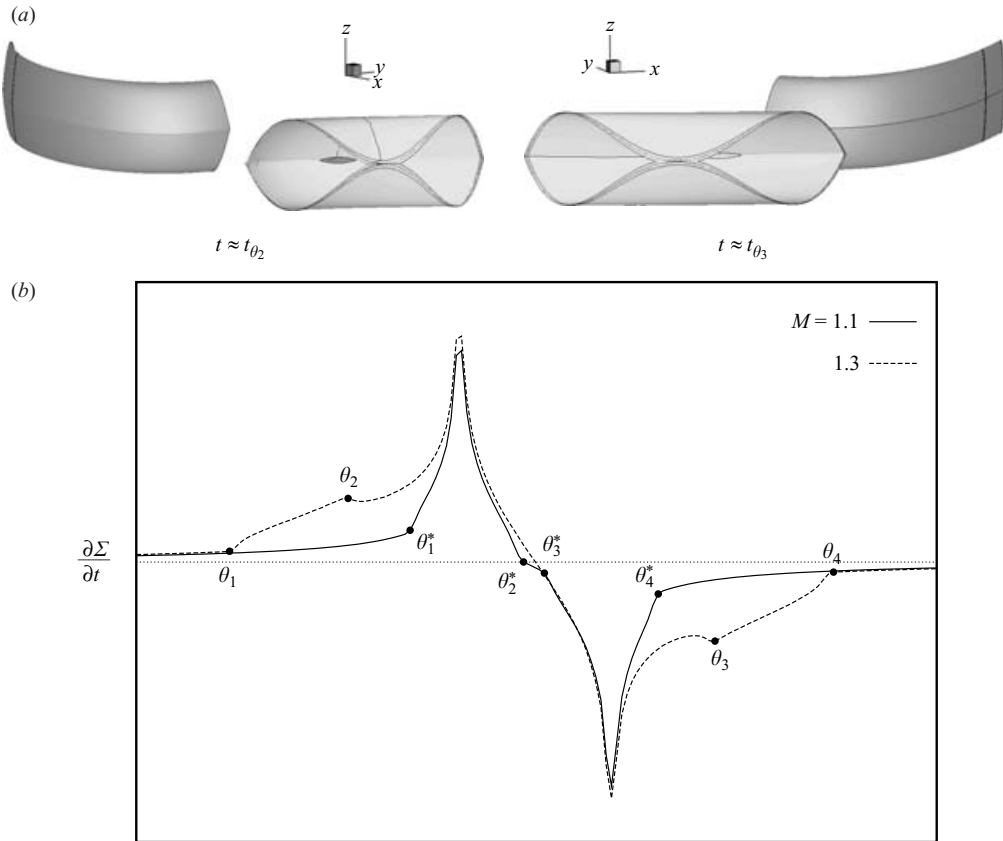


FIGURE 23. (a) The configurations of the Σ surface at the near-singular time steps t_{θ_2} and t_{θ_3} at $\hat{M}_{tip} = 1.3$. (b) The first time derivative of the $\Sigma(t)$ function for the porous surface S_A rotating at $\hat{M}_{tip} = 1.1$ and 1.3 and the shift of the corresponding near singular points along the time axis.

both cases the fluctuations are of a numerical nature and do not have any physical meaning.

Unfortunately, it is not possible to carry out a real noise prediction at supersonic speed for the UH-1H rotor because suitable aerodynamic data is not available. Nevertheless, this numerical investigation shows the favourable aspects of the emission-porous surface formulation in the numerical treatment of such critical operating conditions. Whatever the actual meaning of the \mathcal{T}_1 integral could be, this approach provides an estimation of the acoustic pressure by avoiding any direct integration upon the body, which is a source of a singular behaviour on its own. This feature notably simplifies the calculations and, above all, the proper interpretation of the numerical results.

4.3. The Σ_Λ formulation

The choice of the integration domain S_p of equation (2.9) is a very important issue. In principle, the only requirement is to account for all the nonlinear sources in order to achieve a converged solution. In practice, many other parameters can affect this choice, such as the accuracy or availability of CFD input data or the dangerous effects of the Λ singularity and the attempts to suitably manage them. We have

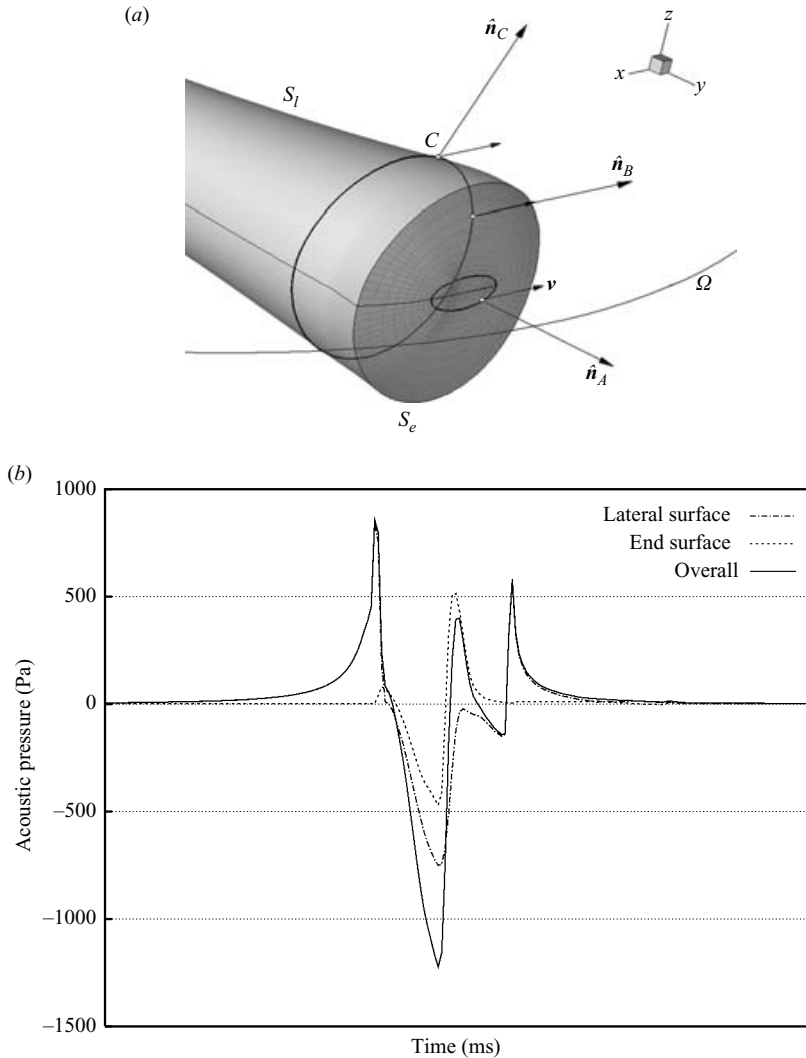


FIGURE 24. (a) At the generic source point A on the end surface S_e the local velocity \mathbf{v} is orthogonal to the outward normal vector $\hat{\mathbf{n}}_A$; thus, M_n is zero and $\Lambda = 1$. (b) The same noise signature as in figure 13 split into the contributions from lateral and end surfaces of the integration domain.

seen also that the shape of the S_p cross-section can have a notable influence on the numerical results. At first glance, the most reasonable choice appears to be the use of a cylindrical domain as close to the blade as possible while including all the transonic effects. Morgans *et al.* (2005) used such a domain to solve equation (2.8) for conditions below the delocalization Mach number, with the aim of limiting the computational effort and assuring the achievement of a converged numerical solution. Nevertheless, this choice may not be the best, especially when the contribution from supersonic sources must be taken into account.

Figure 24(a) shows three different source points placed on a cylindrical mesh. Points B and C are located on a spanwise section of the lateral surface S_l and are related to the outward normal vectors $\hat{\mathbf{n}}_B$ and $\hat{\mathbf{n}}_C$, respectively. Point A belongs to the end

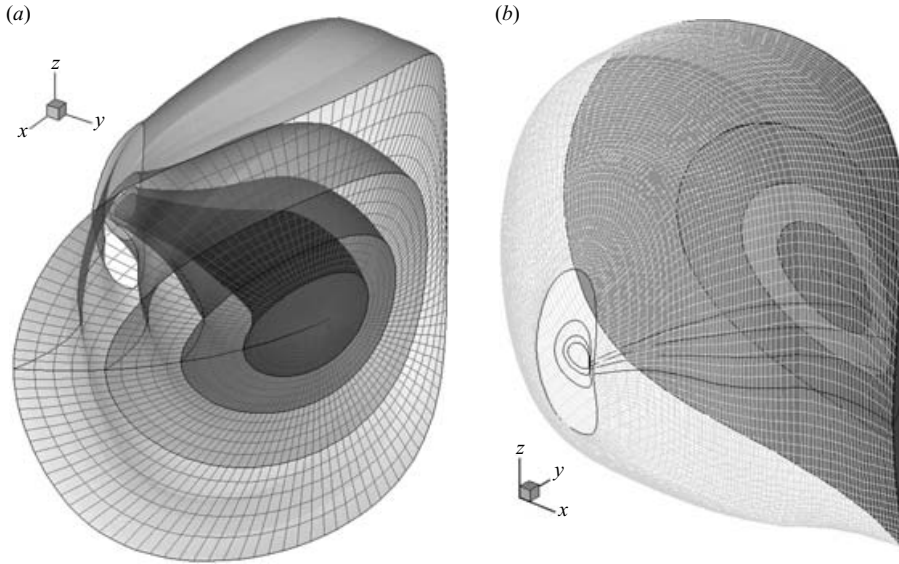


FIGURE 25. The lateral surfaces S_l and (b) the end surfaces S_e used as integration domains and providing the noise predictions of figures 18 and 26.

surface S_e and is associated to the outward normal vector \hat{n}_A . Furthermore, on the Ω trajectory, the direction of rotation is shown so that the \mathbf{v} vector represents the local velocity. The value of M_n at points B and C depends on the rotational velocity and the local angle between \hat{n} and \mathbf{v} ; on the contrary, at point A , M_n is always zero since the local outward normal \hat{n}_A is perpendicular to \mathbf{v} . Thus, at all points placed on a surface characterized by an outward normal direction orthogonal to the local velocity, M_n is zero and, consequently, $\Lambda = 1$. This condition is satisfied well by the end surface S_e of the adopted CFD mesh. Figure 24(b) shows the same overall noise signature of figure 13 (with the integration domain corresponding to the mesh boundaries $k = 15$ and $j = 70$) split into the two contributions from the lateral and end surfaces of the mesh. The spurious peak values due to the Λ singularity affect only the signature from the lateral surface, while the contribution from S_e exhibits a smooth waveform completely free from any singular behaviour. This result provides a very attractive suggestion. Looking at equations (2.6) and (2.7) it is possible to recognize a fundamental aspect of the operators U_i and L_i . By moving the integration domain far enough from the blade both these operators tend to zero, since they approach the conditions of the undisturbed medium. Thus, the density ratio ρ/ρ_0 tends to 1, the pressure p approaches the reference value p_0 (so that $P_{ij} = (p - p_0)\delta_{ij}$ becomes zero) and the fluid is at rest ($u_i = 0$). Then, from a theoretical point of view, the dangerous effects from Λ can be simply (but rigorously) removed by using an integration domain characterized by all nodes with $M_n = 0$ and extended along the outward direction until the contribution from the lateral surface S_l is annihilated. We will refer to this particular domain as to S_A .

Figure 25 shows the integration domains used to determine the separate contributions from the lateral (S_l) and end (S_e) surfaces to the noise predictions reported in figure 18. These contributions are shown in figure 26. As expected, by increasing the size of S_l , the noise signature tends to zero: at $k = 35$ the actual acoustic pressure is zero everywhere except at the two nearly infinite pulses due to the Λ singularity

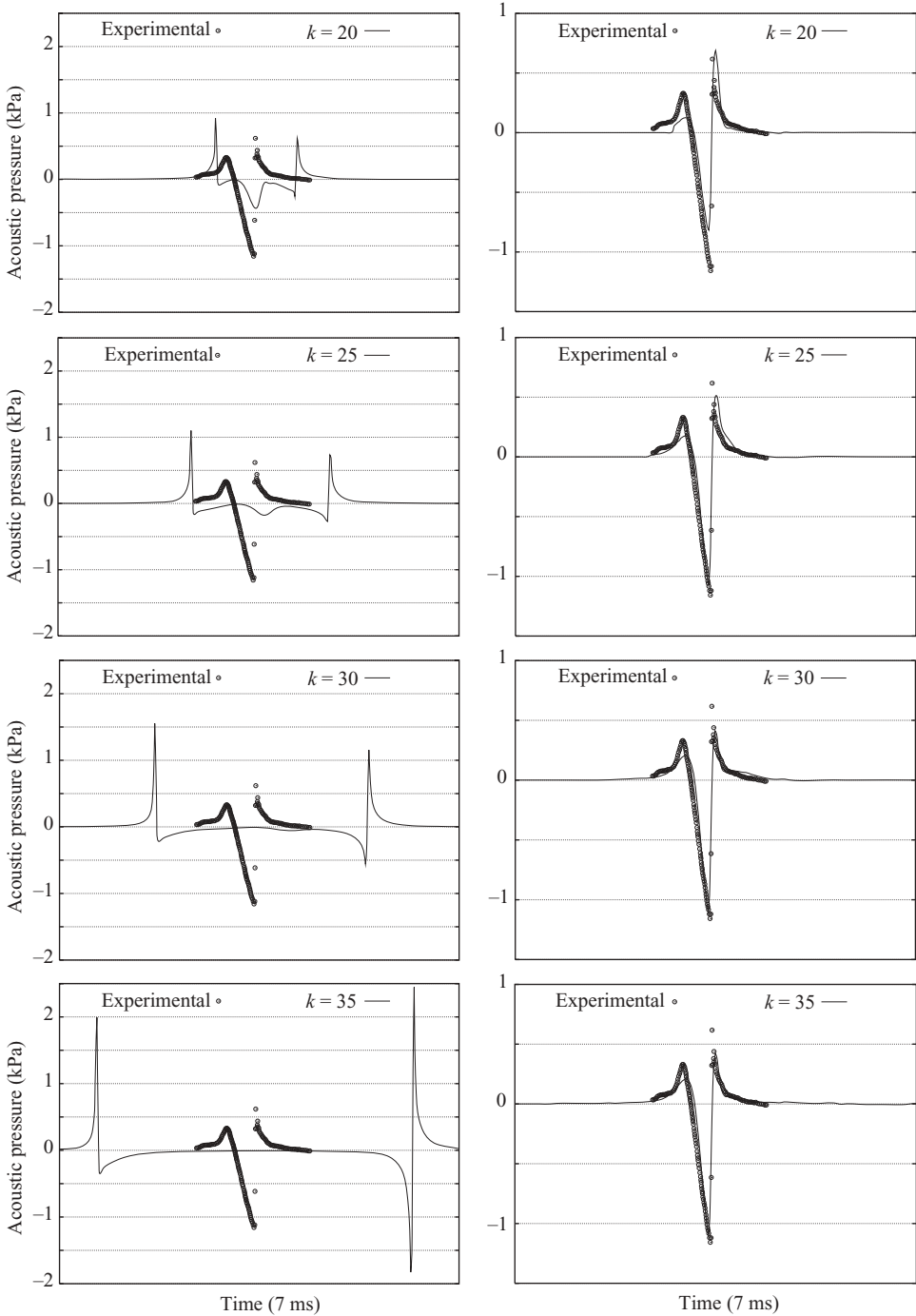


FIGURE 26. The noise contributions provided by the lateral S_l (on the left) and end S_e (on the right) surfaces, corresponding to the different k layers of the CFD mesh. At $k = 35$, the signature from S_l reduces to the spurious pressure peaks due to the Δ singularity, whereas all the contributions provided by S_e highlight the lack of any fictitious fluctuation and a converging behaviour with respect to the experimental data.

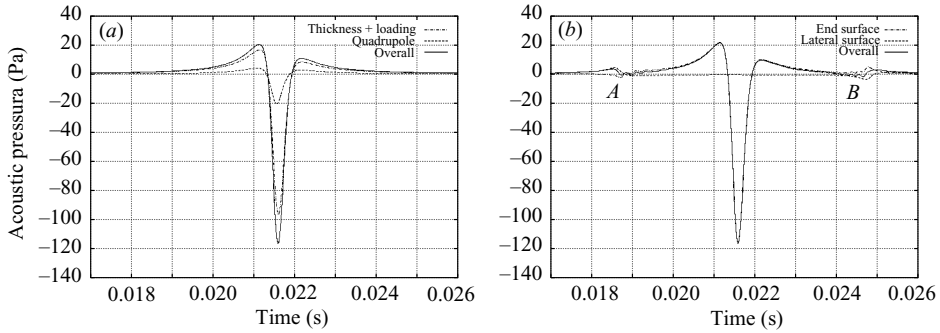


FIGURE 27. Comparison between the numerical solutions of equations (2.2) and (2.8) for the UH-1H hovering rotor at $M_{tip} = 0.85$. (a) The thickness and loading terms are determined through formulation 1A, while the quadrupole noise is computed by a volume integration. Note in (b) the negligible contribution provided by the lateral surface and the slight fluctuations due to the outer spanwise sections.

(figure 26a). On the other hand, the noise contributions provided by the end surfaces S_e only (figure 26b) directly converge towards the experimental data. In practice, the signature corresponding to $k = 35$ exhibits the same waveform as in figure 5, although the time range of computations has been extended in order to highlight the absence of the singular behaviour.

Besides the removal of the Λ effects, the use of the integration domain S_Λ is advantageous from a computational point of view. Accounting for only the end surface S_e notably reduces the size of the emission surface Σ_p and, consequently, the requested CPU time. The comprehensive nature of the contribution provided by the end surface was noted by Delrieux *et al.* (2003). Nevertheless, in that paper the use of an integration domain limited to the end surface S_e (at an intermediate distance from the blade) was erroneously considered to cause an overestimation of the resulting noise signature. The overestimation was probably due to an unsuitable location of the control surface which did not include all the nonlinear effects and thus was not a converged solution.

Concerning the choice of the porous surface, the use of an S_Λ surface is also desirable for solving equation (2.8) where the Doppler singularity urges us to limit the integration domain inside the sonic cylinder. In order to prove this assertion, a condition below delocalization (corresponding to the UH-1H non-lifting hovering rotor at $M_{tip} = 0.85$) has been considered. By exploiting the availability of the same CFD Euler mesh, the integration domain with the boundaries $k = 35$ and $j = 45$ (rotating at a subsonic tip Mach number of approximately 0.9) is used. Figure 27 shows a comparison between the numerical solutions of equations (2.2) and (2.8) at such operating conditions. In figure 27(a), the thickness and loading noise are determined through formulation 1A while the contribution of the quadrupole source terms is obtained through a full volume integration of the aerodynamic data. In figure 27(b), the noise signature is split into contributions from the lateral and the end surfaces, by using the same CFD mesh.

The agreement between the different noise predictions (which match well the experimental data available in the literature, Purcell 1988) is excellent and the contribution from the lateral surface is practically negligible. Furthermore, it is worthnoting that the CPU time requested to perform the volume integration is about 56 s (on a desktop PC), while the signatures from lateral and end surfaces have required 1.79 s

and 1.57 s, respectively. Therefore, by limiting the calculations on the end surface S_e , the computing effort is practically cut in half. Moreover, the prediction of thickness and loading noise has required 1.29 s, a time comparable with the overall noise prediction provided by the integration on S_e . Thus, the use of the porous surface formulation could also be considered as a possible alternative to formulation 1A for linear problems. The slight fluctuations affecting the noise prediction in figure 27(b) represent the numerical instabilities due to the Doppler factor and the contribution from the spanwise outer region. They correspond to the azimuth locations where the emission surface first broadens (by changing the curvature of its leading edge, zone A) and then narrows (by changing the curvature of its trailing edge too, zone B).

In practice, even at subsonic speed, by approaching the sonic cylinder, the sources progressively lose the acoustically compact status, and the Σ surface suffers a notable enlargement. Here, the integrals are not computed on the emission surface, but the numerical solution suffers the effects of the high speed of the outer sources through the presence of the $|1 - M_r|$ singularity. The numerical results of figure 28 (b) concern the noise predictions provided by equation (2.8) by three different integration domains, corresponding to the S_e end surfaces in figure 28(a) and rotating at a tip Mach number of 0.86, 0.90 and 0.95, respectively. At the highest value of the rotational velocity, the noise waveform is characterized by significant fluctuations, very similar to those described in Ianniello (1999b) and also affecting the numerical results provided by the volume integration technique. The use of the emission surface formulation allows the removal of these oscillations since the critical behaviour of the high-speed sources can be modelled in a more accurate way by simply using a finer mesh. Figure 28(c) shows a comparison between the numerical solutions of equations (2.8) and (2.9) (here denoted by RTF and ESF, respectively) obtained by using the same integration domain (the S_e surface at $\hat{M}_{tip} = 0.95$). Although a notable increase in required CPU time (390 s), the noise prediction provided by the integration on the Σ surface is notably smoother and almost free from any numerical instability. This result confirms that by approaching the sonic cylinder, the robustness and reliability of the emission surface approach becomes unquestionably superior with respect to the usual retarded time formulation.

Note that the use of an S_A integration domain allows us to write equation (2.9) in the form

$$4\pi p'(\mathbf{x}, t) = \frac{\partial}{\partial t} \int_{\Sigma_A} \left[\frac{\rho_0 U_n}{r} \right]_{\tau} d\Sigma_A + \frac{1}{c_0} \frac{\partial}{\partial t} \int_{\Sigma_A} \left[\frac{L_r}{r} \right]_{\tau} d\Sigma_A + \int_{\Sigma_A} \left[\frac{L_r}{r^2} \right]_{\tau} d\Sigma_A, \quad (4.3)$$

where, of course, Σ_A represents the emission surface corresponding to S_A . In the following, we will refer to equation (4.3) as to the Σ_A -formulation. This equation represents a singularity-free expression and unlike the Farassat formulations 3 and 4 exhibits a very simple structure. In practice, it reduces the problem of HSI noise prediction to the problem of modelling the Σ_A domain. Within this context, it is worth noting that the shape of the S_A porous surface is important, and neglecting the contribution from the lateral surface S_l is not always appropriate. For instance, at a low-speed BVI condition, where the noise radiation is highly directional and out of the rotor plane, the use of an integration domain surrounding the blade is an advisable (and probably unavoidable) choice. On the contrary, at high speeds and delocalized conditions, the features of Σ_A concerning the extent and the $M_n = 0$ condition are very useful and notably simplify the noise predictions.

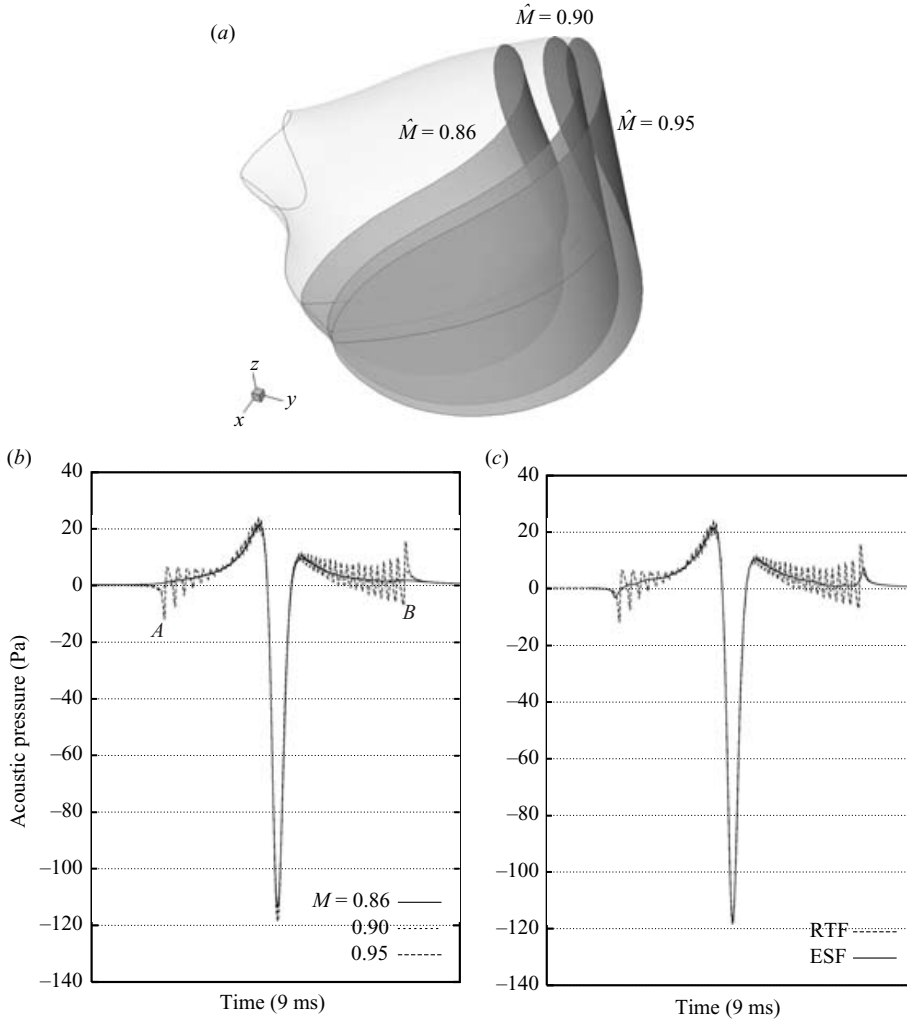


FIGURE 28. Comparison between the noise predictions for the UH-1H hovering rotor at $M_{tip} = 0.85$ achieved by using the three different control surfaces reported in the top figure. They correspond to an increasing spanwise coordinate, which is equivalent to an increasing rotational Mach number M . Note how the use of the emission surface formulation (ESF) removes the numerical instabilities affecting the retarded time formulation (RTF) and due to the outer high-speed sources.

4.4. Old strategies, new perspectives

The results of the previous sections prove the effectiveness and capability of the emission-porous surface formulation in the numerical prediction of noise. It has been shown that a suitable choice of the integration domain can rigorously remove the effects of the Λ singularity, so that equation (4.3) represents a comprehensive solution to the problem of the HSI noise prediction at any range of rotational velocity. All the same, this method requires the modelling of a supersonic emission surface and a computational effort not comparable with the usual solving approaches used at subsonic speed. Even though the use of an S_A surface allows us to cut off the contribution from the lateral surface S_l , the accuracy required to model the Σ_A surface

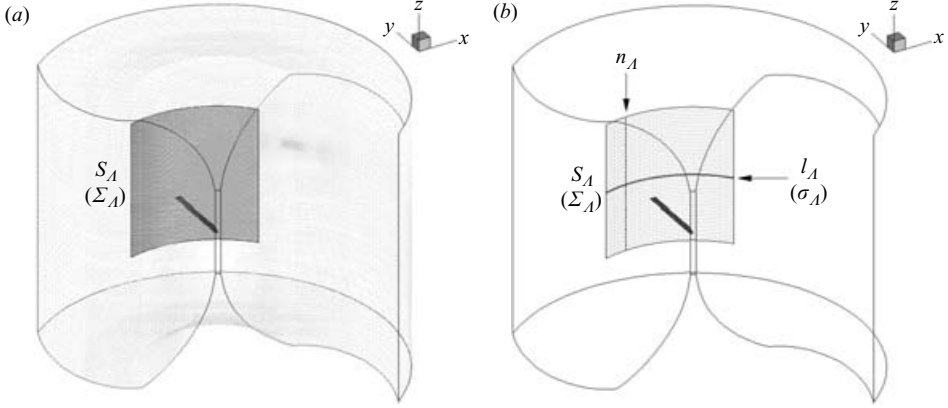


FIGURE 29. (a) A simple S_A surface, formed by a cylindrical open surface placed outside the sonic cylinder and with a size of 2 m along the Z -axis. (b) The intersection of this surface with the rotor plane provides the l_A line and the corresponding n_A normal direction of equations (4.4).

usually calls for a fine mesh and, consequently, a notable CPU time. At this stage, an intriguing suggestion arises from the far-field approximation. Given that all the aerodynamic data carrying out the noise signature are confined on the S_A surface, the use of a preliminary integration along a suitable direction lying on S_A should allow us to achieve an estimation of the overall noise through a simple line integral. Then, following the same approach used by Brentner to define the quadrupole source strength of equation (2.4), we assume

$$\mathcal{U}_i = \int_{n_A} U_i \, dn_A, \quad \mathcal{L}_i = \int_{n_A} L_i \, dn_A \quad (4.4)$$

as the pseudothickness and pseudoloading source strength, and rewrite equation (4.3) in the following form

$$4\pi p'(x, t) = \frac{\partial}{\partial t} \int_{\sigma_A} \left[\frac{\rho_0 \mathcal{U}_n}{r} \right]_{\tau} \, d\sigma_A + \frac{1}{c_0} \frac{\partial}{\partial t} \int_{\sigma_A} \left[\frac{\mathcal{L}_r}{r} \right]_{\tau} \, d\sigma_A + \int_{\sigma_A} \left[\frac{\mathcal{L}_r}{r^2} \right]_{\tau} \, d\sigma_A. \quad (4.5)$$

For clarity, figure 29 shows the fundamental quantities of equations (4.4) and (4.5). A cylindrical open surface (figure 29a), approximately located at the mesh boundaries corresponding to a converged solution ($k=35$ and $j=70$), represents the S_A surface. This domain intersects the rotor plane along the l_A line (figure 29b) so that the pseudothickness and pseudoloading source strength are determined (at each point on l_A) by performing an integration along the normal direction n_A . Of course, the Σ_A and σ_A integration domains represent the emission surface and the emission line corresponding to S_A and l_A , respectively. Equation (4.5) suffers the well-known limits of the far-field approximation (rigorously valid at in-the-rotor-plane and far-field observer locations), but exhibits two attractive features. First, it allows the computation of the acoustic pressure time history through a simple line integration. Even though an overall estimation of the CPU time should also concern the pre-processing of the aerodynamic data, the computational effort becomes very limited compared to the usual solving approaches. Secondly, equation (4.5) does not require the modelling of an emission surface. When the contribution from supersonic sources is significant, the σ_A integration domain must be suitably modelled outside the sonic cylinder with a correct reordering of the retarded source points. Such a task can

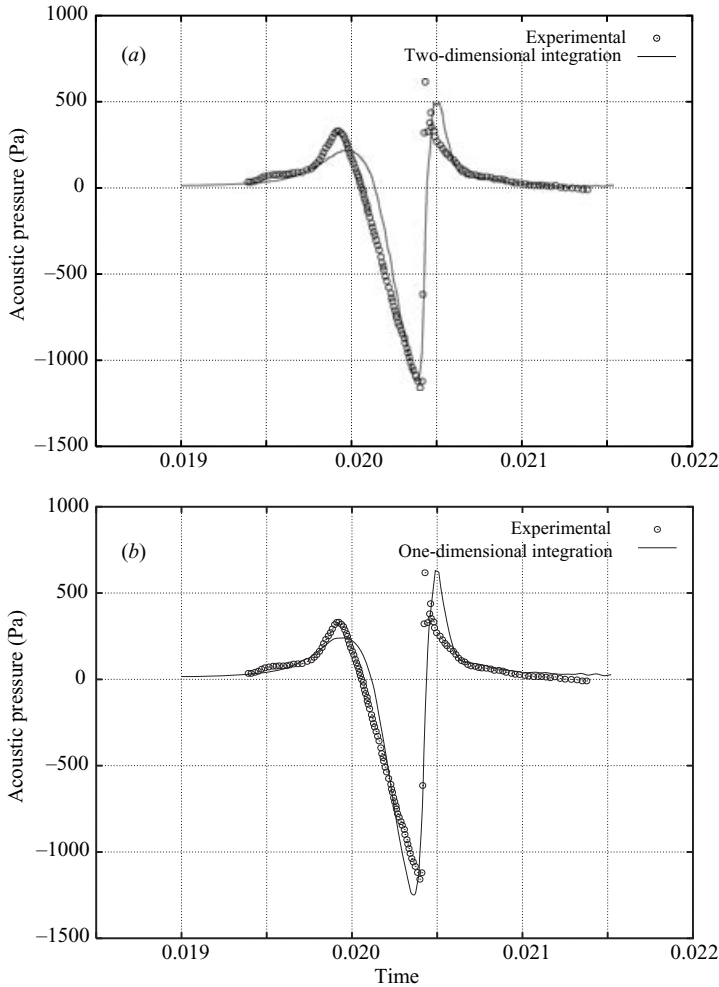


FIGURE 30. Noise predictions provided by equations (a) (4.3) and (b) (4.5), for the UH-1H hovering blade at $M_{tip} = 0.95$. The general agreement of the simple one-dimensional integration scheme with the experimental data is very satisfactory, despite a slight overestimation of the acoustic pressure.

be achieved successfully by using the same identification criteria implemented in the \mathcal{H} -algorithm, but is notably simpler than modelling an emission surface, where a regular mesh must be determined at each time step.

In order to test the capability of equation (4.5) in noise prediction, the trilinear data-fitting procedure has been used to take the requested aerodynamic data from the CFD mesh to the cylindrical open surface figure 29(a). Then, a simple integration routine (based on the Simpson rule) has been used to determine the \mathcal{U}_i and \mathcal{L}_i quantities of equations (4.4). A 50×150 mesh (number of integration lines \times number of nodes on each line) symmetrically placed with respect to the rotor disk is used. The extension along the outward normal direction covers 2m and corresponds to the converged solutions presented in the previous sections. The numerical solutions of both equations (4.3) (two-dimensional-integration) and (4.5) (one-dimensional-integration) are reported in figure 30 for the in-plane observer located at $3.09R$. The comparison with the experimental data shows that the integration upon the

Σ_Δ surface (figure 30a) provides the expected signature, free from any fictitious fluctuation and corresponding to the noise prediction of figure 5(b). On the contrary, the integration upon the σ_Δ line (figure 30b) gives a slight overestimation of the acoustic pressure, despite a general good agreement with the experimental data. This overestimation is due to the restrictions of the far-field approximation. In fact, the collapse of the aerodynamic data along the n_Δ direction presumes the equality of the emission times at source points symmetrically placed with respect to the rotor plane.

At the same time, the observer must be located far enough from the body in order to consider the n_Δ line as a dot-shaped source. The S_Δ surface in figure 29 fully satisfies the first assumption. Nonetheless, the l_Δ line of figure 29(b) can hardly be considered as a set of dot-shaped sources by an observer located at only 3 radii from the rotor hub. Such an approximation becomes valid by increasing the blade–observer distance. Figure 31 shows the comparison between the noise predictions provided by equations (4.3) and (4.5), by progressively moving the location of the in-plane observer away from the blade, up to a distance of 2, 5, 15 and 30 m from the rotor hub. At only 2 m, the difference between the noise predictions is considerable and still the solution from the one-dimensional-integration scheme appears overestimated with respect to the two-dimensional-integration result. On the contrary, at a reasonable distance from the blade (greater than $10R$), the numerical predictions of noise match perfectly.

This result confirms the effectiveness of equation (4.5). Furthermore, the comparison between the CPU time required to achieve the overall noise predictions in figure 30 is impressive. The computation of 256 steps (at a time resolution of 2048 steps per period) required 208.5 and 1.1 CPU seconds for equations (4.3) and (4.5), respectively. Thus, despite the restrictions mentioned, the use of the far-field approximation provides a reduction of the computing costs of two orders of magnitude.

5. Conclusions

The results presented in this paper prove the effectiveness of the emission-porous surface formulation in the prediction of noise from rotating blades. This numerical approach allows us to evaluate the contribution of multi-emissive sources at high-delocalized conditions and removes any limitation on the blade rotational velocity. The robustness of the new \mathcal{H} -algorithm in modelling a supersonic emission surface has been severely tested on complex and anomalous configurations. The availability of such a reliable tool enables the investigation on the behaviour of the Δ singularity affecting the acoustic integrals at supersonic speeds. This analysis confirms the numerical nature of the singularity, reveals its own effects on noise predictions and suggests a practical way to remove them. A general discussion on the numerical solution of the FW-H equation at supersonic speed and the physical meaning of the integral terms is addressed. The evaluation of the pseudo-thickness component of equation (2.9) and the comparison with previous computations of what is addressed as a ‘supersonic thickness noise’ seem to confirm that, approaching the speed of sound, the numerical solution of the FW-H equation has to be pursued globally, since the different integrals lose their physical meaning. Through a strategic choice of the integration domain (aimed at removing the numerical singularities), the Σ_Δ formulation has been proposed. This approach makes the HSI noise prediction straightforward and, like formulation 1A for linear problems, reduces the estimation of the acoustic pressure field to a simple post-processing of the aerodynamic data, regardless of the range of the rotational velocity. Furthermore, for in-plane and far-field observer locations,

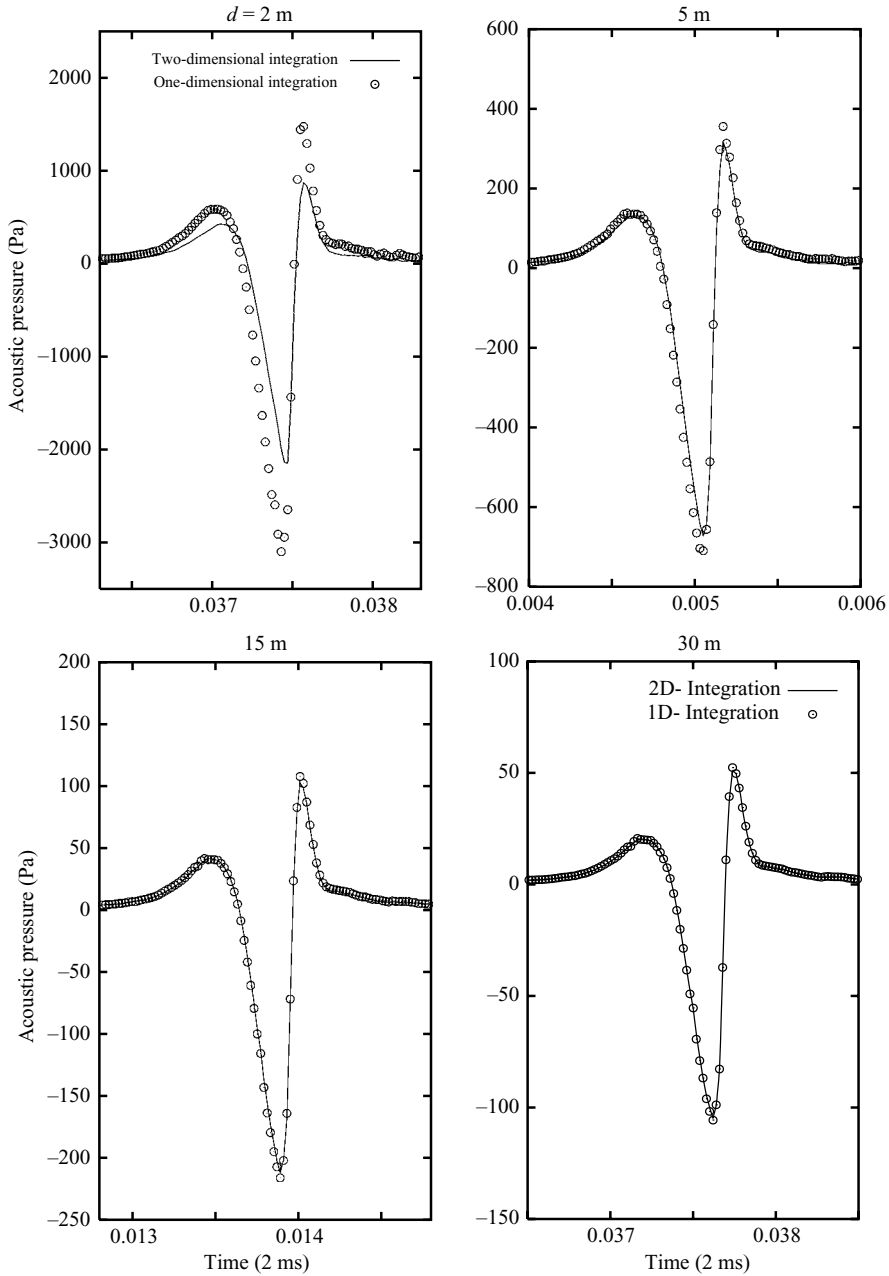


FIGURE 31. The comparison between the noise predictions provided by the Σ_A (two-dimensional) and σ_A (one-dimensional) formulations confirms both the validity and the restrictions of the far field approximation. In the actual far field, the different numerical solutions match perfectly.

the coupling of the Σ_A formulation with the far-field approximation can be used to avoid the construction of the emission surface and provides a reliable noise prediction through a simple one-dimensional integration that is computationally efficient.

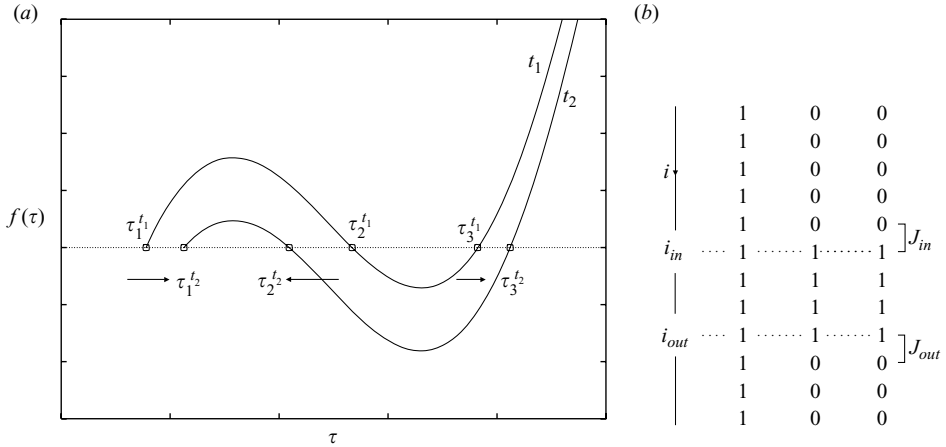


FIGURE 32. (a) The $f(\tau)$ curves of a supersonic source at two subsequent ($t_2 > t_1$) observer times. Note the mid-root τ_2 and the opposite sign of both $\dot{f}(\tau_2)$ (with respect to \dot{f} at the other two roots) and the time interval ($t_2 - t_1$) with respect to $(\tau_2^{t_2} - \tau_2^{t_1})$. (b) A section map of class $C = 2$ highlighting the two jumps J_{in} and J_{out} in the ordered sequence of nodes, at the i_{in} and i_{out} values of the i (chordwise) index.

Appendix. The numerical construction of Σ

This Appendix summarizes the main features of the \mathcal{H} -algorithm, by focusing the attention on the techniques developed to construct the retarded configuration of a curve in a three-dimensional space. Within this context, we will denote such a curve as the *section* \mathcal{S} in order to remind us of the generical (spanwise) section of a structured mesh (see §2) and indicate $\Sigma_{\mathcal{S}}$ as its retarded configuration. The adopted backward-in-time integration scheme requires, at each observer time t , the evaluation of the emission times τ through the well-known equation:

$$f(\tau) = \tau - t + \frac{r}{c_0} = \tau - t + \frac{|\mathbf{x}(t) - \mathbf{y}(\tau)|}{c_0}. \quad (\text{A } 1)$$

The $f(\tau)$ curves of a multi-emissive supersonic source at two subsequent observer times $t_2 > t_1$ (figure 32a) reveal some important issues. Unlike the external roots τ_1 and τ_3 , the mid-root τ_2 exhibits a negative sign for the first time derivative $\dot{f} = \partial f / \partial \tau$ and moves in the opposite direction with respect to the time axis. This last feature provides a sort of contra-rotating motion of the corresponding retarded point $\mathbf{y}(\tau_2)$. On the contrary, no essential feature distinguishes τ_1 and τ_3 . As explained in a previous paper (Ianniello 1999a), within the time interval corresponding to the maximum noise emission, these external roots are characterized by an opposite sign of the second time derivative $\ddot{f} = \partial^2 f / \partial \tau^2$, which is related to a change of curvature in the emission surface. The first version of the \mathcal{H} -algorithm used this feature to model the retarded configuration of each spanwise section. Unfortunately, the sign of \ddot{f} changes twice in a revolution period, so that the procedure fails in constructing the retarded domain in the whole range $[0, 2\pi]$ or when a very large domain is taken into account. Thus, we have to establish a more general criterium to locate the retarded points correctly and construct $\Sigma_{\mathcal{S}}$.

A.1. The section map and the identification criteria

Let us indicate with $m(=3)$ the maximum number of emission times, N the number of ordered nodes of the section \mathcal{S} and i the index which covers \mathcal{S} from 1 to N . At

this stage, we can focus attention on a open section, where the nodes i_1 and i_N are univocally identified; nevertheless, the numerical treatment of a closed section may be derived easily from the open one. For a supersonic section \mathcal{S} , we suppose that we have all the emission times and the corresponding retarded spatial coordinates available at a fixed observer time t . These values can be efficiently determined by solving equation (A 1) through the *crossed iteration scheme* (Ianniello 2001).

The retarded configuration $\Sigma_{\mathcal{S}}$ can be associated to a flag array ($N \times m$), whose elements are equal to 1 (or 0) depending on the existence (or not) of the emission time. This array is named a *section map* and exhibits the following features: (a) all the elements of the first column are equal to 1; (b) at each row, the elements of the second and third columns must be the same. These features arise because equation (A 1) always exhibits one or three roots. The section map represents a useful working-tool and holds some fundamental information about the topology of $\Sigma_{\mathcal{S}}$. Its elements act as pointers to the fundamental arrays of the emission times τ and retarded coordinates \mathbf{y} . Moreover, they enable the identification of the possible jumps between two subsequent supersonic sources experiencing (at fixed t) a different status. These jumps point out the occurrence of a transition region within $\Sigma_{\mathcal{S}}$ and the need for a suitable reordering of the retarded coordinates. Because of the importance of the role, the number of jumps in the section map has been named the *class* (C) of the section.

In order to understand how the map can be used to construct $\Sigma_{\mathcal{S}}$, let us consider a section composed by only twelve nodes and characterized, at a fixed observer time t , by the section map shown in figure 32(b). The section includes one multi-emissive region (4 nodes) and the map identifies two jumps ($C = 2$) within the ordered sequence of nodes corresponding to the two indices i_{in} and i_{out} of the boundary (multi-emissive) sources. The criterium used to establish how to locate the retarded coordinates \mathbf{y} is based on a sort of time-continuity assumption. The question is: ‘within $\Sigma_{\mathcal{S}}$, what is the *next* point with respect to the (single-emissive) node $\mathbf{y}_{i_{in}-1}$ and the *previous* point with respect to (single-emissive) node $\mathbf{y}_{i_{out}+1}$?’ Because of the mentioned contra-rotating motion, the nodes corresponding to the mid-root $\mathbf{y}(\tau_2)$ are left out. The remaining choice between $\mathbf{y}(\tau_1)$ and $\mathbf{y}(\tau_3)$ (both at input and output jump) is governed by the emission phenomena so that the correct selection corresponds to the retarded source with the emission time closer to the next/previous single-emissive node. Thus, at the jump points identified by the section map, the following link-parameters are determined:

$$J_{in} : \begin{cases} \mathcal{L}_1^{in} = |\tau_{i_{in}}^1 - \tau_{(i_{in}-1)}|, \\ \mathcal{L}_2^{in} = |\tau_{i_{in}}^3 - \tau_{(i_{in}-1)}|, \end{cases} \quad J_{out} : \begin{cases} \mathcal{L}_1^{out} = |\tau_{i_{out}}^1 - \tau_{(i_{out}+1)}|, \\ \mathcal{L}_2^{out} = |\tau_{i_{out}}^3 - \tau_{(i_{out}+1)}|, \end{cases} \quad (\text{A } 2)$$

where the superscript for τ denotes the column of the section map and, correspondingly, the number of the $f(\tau)$ root. The identification criteria mentioned correspond to the following three different cases:

- (i) $\mathcal{L}_1^{in} < \mathcal{L}_2^{in}$ and $\mathcal{L}_1^{out} < \mathcal{L}_2^{out}$.

In this case, $\mathbf{y}(\tau_{in-1})$ connects to $\mathbf{y}(\tau_{in}^1)$ and $\mathbf{y}(\tau_{out+1})$ to $\mathbf{y}(\tau_{out}^1)$ and the multi-emissive sources give rise to an unconnected patch. Generally, such a situation corresponds to the early occurrence of a multi-emissive status of the supersonic sources and the separate region is destined to grow.

- (ii) $\mathcal{L}_1^{in} > \mathcal{L}_2^{in}$ and $\mathcal{L}_1^{out} > \mathcal{L}_2^{out}$.

In this case, $\mathbf{y}(\tau_{in-1})$ connects to $\mathbf{y}(\tau_{in}^3)$ and $\mathbf{y}(\tau_{out+1})$ to $\mathbf{y}(\tau_{out}^3)$. Still, the retarded configuration $\Sigma_{\mathcal{S}}(t)$ exhibits a separate region, but the emission of the sources with

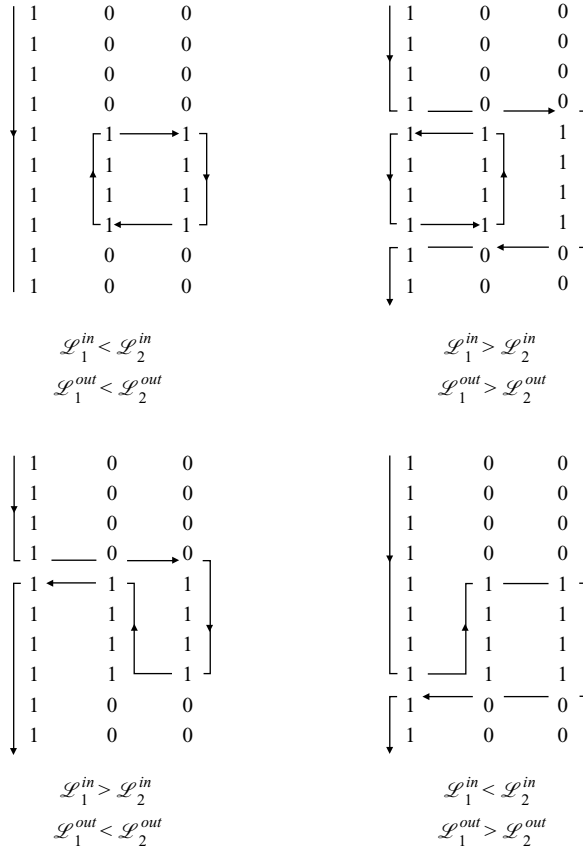


FIGURE 33. A summary of the identification criteria established by the link parameters \mathcal{L} and used to reorder the retarded coordinates y in presence of a multi-emissive branch within the section map.

a single τ is a subsequent event with respect to the emission of the multi-emissive sources. Then, the unconnected patch is going to collapse.

(iii) $\mathcal{L}_1^{in} < \mathcal{L}_2^{in}$ and $\mathcal{L}_1^{out} > \mathcal{L}_2^{out}$ or $\mathcal{L}_1^{in} > \mathcal{L}_2^{in}$ and $\mathcal{L}_1^{out} < \mathcal{L}_2^{out}$.

Here, the link-parameters require the link of $y(\tau_{in-1})$ to $y(\tau_{in}^1)$ and $y(\tau_{out+1})$ to $y(\tau_{out}^3)$ (or $y(\tau_{in-1})$ to $y(\tau_{in}^3)$ and $y(\tau_{out+1})$ to $y(\tau_{out}^1)$), so that the multi-emissive region is inevitably included within sources with a single τ . In both cases, the retarded configuration $\Sigma_{\mathcal{G}}(t)$ represents a single manifold.

A sketch of the section map corresponding to the different cases helps us to understand the order of nodes in $\Sigma_{\mathcal{G}}$ and is shown in figure 33. It is worthnoting that the second column of the map is always swept in a direction opposite to the i index, thus fulfilling the kinematic requirements of the mid-roots τ_2 . The cases shown in figure 33 are relatively simple and correspond to retarded configurations which could be constructed also by the old version of the algorithm. In particular, the cases (i) and (ii) correspond to the so-called *mixed* section, while both cases (iii) represent a *partial* section, as cited in Ianniello 1999a, 2001.

Nevertheless, the proposed identification criteria enable the modelling of much more complex configurations of $\Sigma_{\mathcal{G}}$, characterized by the presence of many unconnected

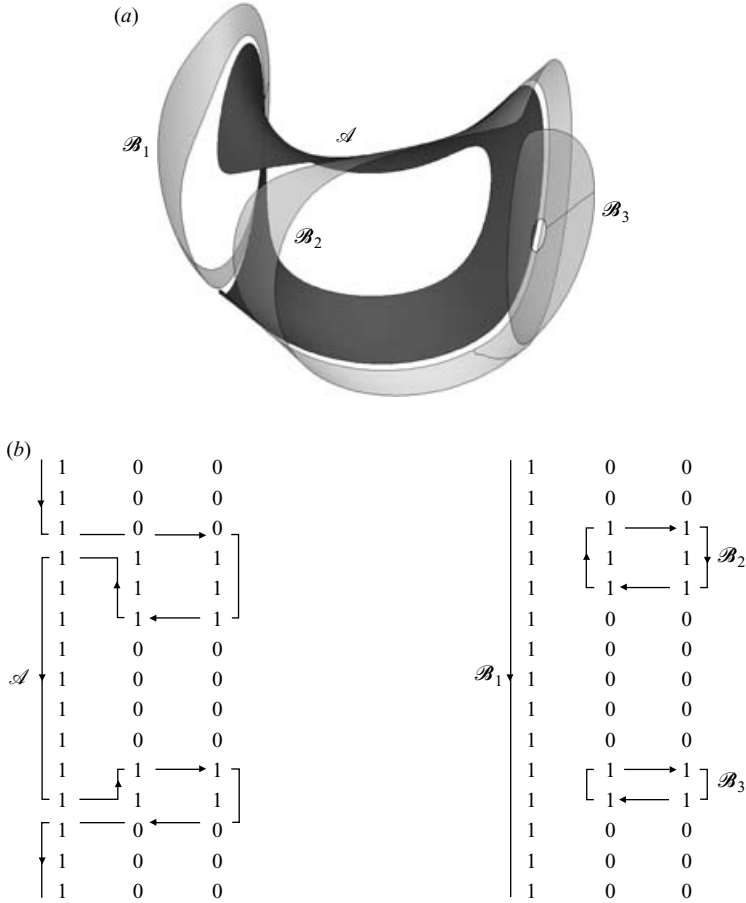


FIGURE 34. All the spanwise sections composing the single region \mathcal{A} and the triple region \mathcal{B}_i (a) are of class $C = 4$; nevertheless, the identification criteria and the link parameters determined on the corresponding section maps (schematically shown in b) provide the different topology of the two regions.

patches. Obviously, the class of section is not sufficient to identify $\Sigma_{\mathcal{G}}$. For instance, figure 34(a) shows two spanwise regions of an emission surface Σ where all the retarded sections have $C = 4$. The corresponding section maps reported in figure (b) clearly show that both the multi-emissive branches can link up with the single-emissive sources in order to constitute a single manifold (dark region, \mathcal{A}), or, alternatively, give rise to three separate strips (light regions, \mathcal{B}_i). Then, the *type* (T) of the section is fixed by its class and the number of unconnected regions arising from the multi-emissive branches, which is determined by the identification criteria. The identification of the type T of $\Sigma_{\mathcal{G}}$ is a fundamental step in the construction of Σ . It enables the assemblage of the retarded sections into homogeneous patches and an effective management of the appearance and disappearance of fragmented regions. Note that the number of retarded nodes y is usually different at subsequent sections so that a data-fitting procedure must be used (on each patch) to achieve a regular mesh and compute the acoustic integrals through a simple zero-order formulation.

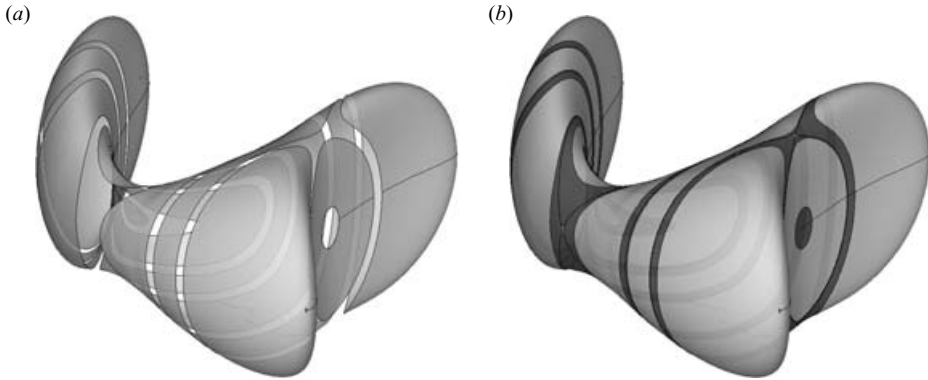


FIGURE 35. (a) A Σ surface of the sphere in figure 1 as determined for the starting mesh 40×101 ; it highlights the need for a spanwise mesh refinement at the transition regions between subsequent patches of different type. (b) The additional patches computed by the spanwise mesh refinement procedure (dark regions).

A.2. The self-adaptive grid

Whatever the resolution of the starting mesh may be, an accurate evaluation of the $\Sigma(t)$ function requires a step-by-step modification of the numerical grid. This task is essential to achieve a reliable prediction of noise and concerns both the spanwise and chordwise grid resolution. Figure 35 shows an emission surface of the sphere of §2 (test-case 1), corresponding to the starting mesh 40×101 . Despite the correct reconstruction of the different patches, it is evident that there is a need for a grid refinement along the ‘span’, at each transition region between two subsequent patches of different type. At any observer time t , this aim is achieved: (a) by locating an additional section between the boundaries of the adjoining patches; (b) by determining the retarded configuration of the new section and the corresponding type T; (c) by assuming the section as the new boundary of the region of the same type T. The procedure is repeated until a prescribed minimum distance between the subsequent patches is obtained. A numerical problem arises if the additional section corresponds to neither type of the neighbouring patches. This condition has been identified as a *blackhole*, since it can be a recursive problem (depending on the grid shape and resolution) and is difficult to manage. The present version of the \mathcal{K} -algorithm is able to treat a blackhole condition of order 3 (where a different T occurs three times during the refinement procedure).

Besides the spanwise grid refinement, a self-adaptive scheme must usually be adopted, also along the ‘chord’ direction. There are two reasons for that. First, the retarded source points tend to run away from the Doppler line $(1 - M_r) = 0$ (Ianniello 1999a) which corresponds to the jumps between multi-emissive and single-emissive sources. This behaviour causes a notable sparseness of nodes, especially in the region overlapping the sonic cylinder. Secondly, the multi-emissive branch occurring in a retarded section can be constituted by only one or two sources. In both cases, the data-fitting (spline-based) procedure devoted to construct the different patches requires some additional points to construct the different patches correctly. Thus, a prescribed number of nodes is added at each jump identified in the section map.

REFERENCES

- AMIET, R. K. 1988 Thickness noise of a propeller and its relation to blade sweep. *J. Fluid Mech.* **192**, 535–560.

- BRENTNER, K. S. 1997 An efficient and robust method for predicting helicopter rotor high-speed impulsive noise. *J. Sound Vib.* **203**, 87–100.
- BRENTNER, K. S. & FARASSAT, F. 1997 An analytical comparison of the acoustic analogy and Kirchhoff formulation for moving surfaces. *AIAA J.* **202**, 491–509.
- BRENTNER, K. S. & FARASSAT, F. 2003 Modeling aerodynamically generated sound of helicopter rotors. *Prog. Aerospace Sci.* **39**, 83–120.
- DELRIEUX, Y., PRIEUR, J., RAHIER, G. & DROUSIE, G. 2003 A new implementation of aeroacoustic integral method for supersonic deformable control surface. *AIAA Paper* 2003–3201.
- DI FRANCESCANTONIO, P. 1997 A new boundary integral formulation for the prediction of sound radiation. *J. Sound Vib.* **202**, 491–509.
- FARASSAT, F. 1981 Linear acoustic formulas for calculation of rotating blade noise. *AIAA J.* **19**, 1122–1130.
- FARASSAT, F. & BRENTNER, K. S. 1988 The uses and abuses of the acoustic analogy in helicopter rotor noise prediction. *J. Am. Helicopter Soc.* **33**, 29–36.
- FARASSAT, F. & BRENTNER, K. S. 1998a Supersonic quadrupole noise theory for high-speed helicopter noise. *J. Sound Vib.* **218**, 481–500.
- FARASSAT, F. & BRENTNER, K. S. 1998b A study of supersonic surface sources – the Ffowcs Williams–Hawkings equation and the Kirchhoff formula. *AIAA Paper* 98-2375.
- FARASSAT, F. & FARRIS, M. 1999 Verification and analysis of formulation 4 of Langley for the study of noise from high speed surfaces. *AIAA Paper* 99–1881.
- FARASSAT, F. & MYERS, M. K. 1988 Extension of Kirchhoff’s formula to radiation from moving bodies. *J. Sound Vib.* **123**, 451–461.
- FARASSAT, F., PEGG, R. J. & HILTON, D. A. 1975 Thickness noise of helicopter rotors at high tip speed. *AIAA Paper* 75–423.
- FARASSAT, F., PADULA, S. L. & DUNN, M. H. 1987 Advanced turboprop noise prediction based on recent theoretical results. *J. Sound Vib.* **119**, 53–79.
- FFOWCS WILLIAMS, J. E. & HAWKINGS, D. L. 1969 Sound generation by turbulence and surfaces in arbitrary motion. *Phil. Trans. R. Soc. A* **264**, 321–342.
- IANNIELLO, S. 1999a An algorithm to integrate the FW-H equation on a supersonic rotating domain. *AIAA J.* **37**, 1040–1047.
- IANNIELLO, S. 1999b Quadrupole noise predictions through the Ffowcs Williams–Hawkings equation. *AIAA J.* **37**, 1048–1054.
- IANNIELLO, S. 2001 Aeroacoustic analysis of high tip-speed rotating blades. *J. Aerospace Sci. Tech.* **5**, 179–192.
- IANNIELLO, S. & DE BERNARDIS, E. 1994 Calculation of high speed noise from helicopter rotors using different descriptions of quadrupole source. *AGARD Symp. on Aerodynamics and Aeroacoustics of Rotorcraft*, Paper 27.
- KUNTZ, M., LOHMANN, D., LIESER, J. A. & PAHLKE, K. 1995 Comparisons of rotor noise predictions obtained by a lifting surface method and Euler solutions using Kirchhoff equation. *AIAA Paper* 95–136.
- LYRINTZIS, A. S. 1994 Review, the use of Kirchhoff’s method in computational aeroacoustics. *Trans. ASME: J. Fluids Engng* **116**, 665–676.
- MORGANS, A. S., KARABASOV, S. A., DOWLING, A. P. & HYNES, T. P. 2005 Transonic helicopter noise. *AIAA J.* **43**, 1512–1524.
- PURCELL, T. W. 1988 CFD and transonic helicopter sound. *14th European Rotorcraft Forum*, Paper 2.
- STRAWN, R. C., BISWAS, R. & LYRINTZIS, A. S. 1996 Helicopter noise predictions using Kirchhoff methods. *IMACS J. Comput. Acoust.* **4**, 321–339.
- WELLS, V. L. 1988 Analysis of the acoustic planform method for rotor noise prediction. *AIAA J.* **26**, 522–523.
- WELLS, V. L. 1991 Acoustic waveform singularities from supersonic rotating surface sources. *AIAA J.* **29**, 387–394.
- WELLS, V. L. & HAN, A. 1993 Geometrical and numerical considerations in computing advanced-propeller noise. *J. Aircraft* **30**, 365–371.
- YU, Y. H., CARADONNA, F. X. & SCHMITZ, F. H. 1978 The influence of the transonic flow field on high-speed helicopter impulsive noise. *4th European Rotorcraft and Powered Lift Aircraft Forum*, Paper 58.